International Journal of Engineering Science 228 (2026) 104638

Contents lists available at ScienceDirect

International Journal of Engineering Science

journal homepage: www.elsevier.com/locate/ijengsci

Full length article

Strain localization in softening plasticity without modifying standard constitutive models: A deformable Cosserat approach

Andrea Panteghini [a,*], M.B. Rubin [b]

[a] Department of Civil, Environmental, Architectural Engineering and Mathematics (DICATAM), Università degli Studi di Brescia, Italy
[b] Faculty of Mechanical Engineering, Technion-Israel Institute of Technology, 32000 Haifa, Israel

ARTICLE INFO

Keywords:
Strain localization
Strain softening
Elastoplasticity
Cosserat continuum
Internal length scale
Mesh independence

ABSTRACT

This paper presents a formulation for strain localization in softening plasticity based on a deformable Cosserat model. The approach enables the direct use of standard elastoplastic constitutive models formulated for a classical Cauchy continuum, without any modification of the stress update algorithm or the local material consistent tangent operator provided by the underlying constitutive routine. The key feature of the proposed framework is a strict separation between dissipative and energetic mechanisms: all dissipation is confined to the macro-continuum, while the micro-continuum contributes exclusively through linear elastic terms associated with the director field. As a result, the constitutive structure of the underlying elasto-plastic model is preserved, and any standard small deformation, thermodynamically consistent constitutive model can be employed as a black-box stress-update module. The internal length scale arises naturally from the micro-continuum and governs the development, interaction, and selection of localization patterns, rather than acting as a diffusive or artificial parameter. The formulation is straightforward to implement within standard finite element frameworks: the local constitutive integration is left unchanged, while the global residual vector and tangent matrix are augmented by the additional linear contributions associated with the director field. The performance of the proposed approach is assessed through benchmark problems involving shallow foundations on soil, which represent a particularly demanding test due to the onset of complex, interacting, and unstable localization mechanisms. Both Tresca and Matsuoka–Nakai plasticity models are considered, including cases exhibiting highly unstable post-peak responses. Numerical results show that load–displacement responses, dissipated energy, and shear-band patterns converge upon mesh refinement, even in the presence of strongly nonlinear and interacting localization processes. These findings indicate that the proposed framework provides a promising route for mesh-objective analyses of strain localization in softening plasticity, while preserving the constitutive structure of the underlying elastoplastic model.

1. Introduction

Elasto-plastic constitutive models within the classical Cauchy continuum are widely used for the analysis of structural and geotechnical problems. However, capturing key features of material behavior – particularly for geomaterials – often requires the introduction of strain softening, which leads to severe numerical and theoretical difficulties.

In the presence of strain softening, the governing boundary value problem may lose ellipticity, which manifests itself in numerical simulations as pathological mesh sensitivity. In particular, computed responses do not converge upon mesh refinement,

* Corresponding author.
E-mail addresses: andrea.panteghini@unibs.it (A. Panteghini), mbrubin@tx.technion.ac.il (M.B. Rubin).

https://doi.org/10.1016/j.ijengsci.2026.104638
Received 15 June 2026; Received in revised form 7 July 2026; Accepted 7 July 2026
Available online 14 July 2026
0020-7225/© 2026 The Authors. Published by Elsevier Ltd. This is an open access article under the CC BY-NC-ND license (http://creativecommons.org/licenses/by-nc-nd/4.0/).

and the width of localized deformation bands becomes dependent on the discretization size (see, e.g., de Borst (1991), de Borst and Sluys (1991), Sabet and de Borst (2019a)). These issues directly affect both the reliability and the robustness of numerical analyses: mesh-dependent localization patterns undermine the mechanical significance of the computed response, while severe convergence difficulties may arise and prevent the simulation from being completed as localization develops. These difficulties are now understood as a direct consequence of the loss of well-posedness of the governing equations. In quasi-static problems, the onset of localization is associated with a loss of ellipticity, which underlies both the observed mesh dependence and the severe numerical instabilities (Sabet & de Borst, 2019b).

Several approaches have been proposed in the literature to overcome the pathological mesh dependence associated with strain localization in softening materials.

One class of approaches is based on mechanical enrichments of the Cauchy continuum. For example, the Cosserat continuum, originally introduced by Cosserat and Cosserat (1909), augments the classical kinematics by introducing independent rotational degrees of freedom governed by additional balance equations, thereby incorporating intrinsic length scales into the formulation. In this work, this formulation is referred to as a *rigid Cosserat model*, since the enriched kinematics can be characterized by the rotation of a rigid triad of director vectors. In particular, rigid Cosserat models have long been regarded as a natural framework for the analysis of shear banding, starting from the seminal work of Mühlhaus and Vardoulakis (1987), which showed that the introduction of an intrinsic length scale leads to localization bands of finite thickness. Starting from the pivotal computational studies of de Borst (1991) and Perić et al. (1994), the rigid Cosserat model has been widely employed in numerical analyses and benchmark problems (Khoei & Karimi, 2008; Khoei et al., 2010; Panteghini & Lagioia, 2022a, 2022b; Sabet & de Borst, 2019a; Sharbati & Naghdabadi, 2006), as well as in practical applications involving localization phenomena (Ebrahimian et al., 2012; Russo et al., 2020). However, it is now well recognized that this regularization is only partial: while objective results can be obtained in problems characterized by a single dominant shear band, mesh dependence may reappear when multiple bands nucleate, interact, or evolve sequentially (Duretz et al., 2023; Panteghini & Rubin, 2026).

This class further includes micromorphic models (Eringen & Suhubi, 1964; Forest, 2009, 2020b; Forest & Sievert, 2006; Suhubi & Eringen, 1964), that are closely related but conceptually distinct from the rigid Cosserat. They introduce a fully independent micro-deformation tensor at each material point, thereby allowing for a very general and systematic description of microstructural effects and internal length scales.

A second class of approaches aims instead at restoring well-posedness through explicit regularization of the governing equations. These include gradient-enhanced plasticity and damage models (Anand, 2026; Jirásek, 2003; Lorentz, 2011; Peerlings et al., 1996, 1998), viscoplastic formulations (Needleman & Tvergaard, 1992), and nonlocal approaches based on spatial averaging (Bažant & Jirásek, 2002; Bažant & Pijaudier-Cabot, 1988). More recently, phase-field formulations (Duda et al., 2015; Miehe et al., 2017; Miehe, Hofacker, & Welschinger, 2010; Miehe, Welschinger, & Hofacker, 2010) have gained increasing attention, introducing auxiliary field variables governed by additional differential equations to regularize localization phenomena. While these approaches have proven effective in controlling mesh dependence, they are typically introduced as mathematical regularization techniques, rather than as mechanically enriched continuum models.

A practical difficulty common to many regularized or enriched formulations is that the additional fields often enter directly into the constitutive description, requiring dedicated constitutive equations and implementation strategies. As a consequence, these formulations are not always readily combined with existing elastoplastic models developed for the classical Cauchy continuum and implemented through standard stress-update algorithms.

The framework adopted in this work is based on the deformable Cosserat model recently proposed by Rubin (2025a, 2025b), which enriches the continuum with a triad of deformable director vectors. It was previously shown by Panteghini and Rubin (2026) that, in the context of elasticity with damage, the original formulation is able to predict the mesh- and rate-independent evolution of shear bands, since elastic and total deformations essentially coincide. However, preliminary investigations in the context of elastoplasticity revealed that this property is lost when elastic and total deformations are no longer equivalent, and that the original formulation does not provide a consistent description of localization in this case. For this reason, a modified version of the deformable Cosserat model has been developed for elastoplastic response involving volumetric plastic deformations, and is presented in the companion theoretical paper (Rubin & Panteghini, 2026). It is also noted that, as discussed by Rubin (2026), in the small-deformation setting adopted here, the resulting formulation exhibits strong similarities with classical microstructural models developed by Mindlin (1964). After the reduction to the symmetric director strain, the small-strain formulation employed here can be written in the same form as the microstrain tensor model reviewed by Forest (2016). In that model, the free energy contains quadratic contributions depending on the relative strain between the macro-strain and an independent microstrain tensor, as well as on the gradient of the microstrain. Similar micromorphic or local second-gradient structures have also been used for geomaterial localization (Chambon et al., 2001) and for metallic foams (Dillard et al., 2006). This correspondence should be understood at the level of the small-strain specialization only. The underlying nonlinear deformable Cosserat theory (Rubin & Panteghini, 2026) remains distinct from the nonlinear micromorphic frameworks developed in Forest and Sievert (2006) and Forest (2016, 2020a).

In the deformable Cosserat model, the material comprises two interacting continua: a macro-continuum, which can be described by any standard, small-deformation thermodynamically consistent constitutive model, and a micro-continuum, associated with the evolution of a deformable director triad. The two continua are constitutively uncoupled: the macro-continuum governs the entire dissipative response, while the micro-continuum introduces additional energetic terms associated with the *relative* deformation of the directors with respect to the macro-continuum deformation. These energetic terms become significant in regions of strong strain localization and govern the structure of the emerging deformation patterns.

The key point exploited in the present work is that, in the elastoplastic setting considered here, this microstrain-type regularization mechanism is obtained without modifying the dissipative macro-constitutive law. The standard Cauchy elastoplastic stress-update algorithm and its local material consistent tangent can therefore be retained as black-box constitutive modules, while the additional director-related terms are assembled as energetic contributions to the global residual vector and tangent matrix of the coupled finite element problem.

It should be noted that the enhanced kinematics of the deformable Cosserat model come at the price of additional degrees of freedom compared to the rigid Cosserat model. Nevertheless, the equations associated with these degrees of freedom form a linear-elastic block of the coupled discrete system. In the benchmark problem here investigated, the computational cost is balanced by a substantially stronger regularization capability, since the micro-continuum is activated by strong spatial variations of the deformation field itself, rather than only by rotational mechanisms. A more quantitative comparison of the computational cost of the deformable and rigid Cosserat models has been reported in the recent paper on damage-induced localization by Panteghini and Rubin (2026). Such a comparison is not repeated here, because in the present elastoplastic setting a direct comparison with a rigid Cosserat plasticity model is less straightforward.

The term black-box is used here only in this constitutive sense: the macro-constitutive stress-update algorithm and its local material tangent are not modified. Although the small-strain structure of the present formulation is related to a Helmholtz-type microstrain regularization model, whose properties are well established for suitable quadratic energetic choices (Forest, 2016), this should not be interpreted as a model-independent guarantee of regularization for arbitrary softening laws. The effectiveness of the regularization, the required spatial resolution, and the selected localization patterns may depend on the macro-constitutive model, on the energetic parameters of the director contribution, and on the boundary-value problem.

The objective of the present work is to assess the capability of the deformable Cosserat model to predict strain localization in softening plasticity within a mechanically meaningful setting. In particular, the internal length ℓ is treated as a constitutive material length-scale parameter, rather than as a numerical regularization parameter. Accordingly, it is not adjusted with the mesh size; its experimental identification is material- and problem-dependent and may rely, for instance, on measured shear-band thicknesses or full-field strain profiles in localized deformation tests. Classical biaxial tests specifically designed to allow the spontaneous formation of shear bands in soils, such as those of Vardoulakis and Goldscheider (1981), provide a relevant experimental setting in which such information could be obtained.

For a fixed value of ℓ, the numerical examples considered in this work show mesh-independent solutions converging towards well-defined localization patterns. At the same time, for the benchmarks here analyzed, varying ℓ can lead to qualitatively different responses, both in terms of global behavior and the associated shear band structures. The proposed framework therefore does not merely regularize the solution, but provides a mechanically grounded mechanism for the selection and evolution of localized deformation patterns, while enabling the direct use of standard constitutive models as true black-box components.

2. The deformable Cosserat model

The formulation adopted in this work is the small-deformation specialization of the thermodynamically consistent deformable Cosserat theory developed in the companion paper (Rubin & Panteghini, 2026). The general framework is derived there in an Eulerian large-strain setting, whereas the present paper focuses on the simplified small-deformation equations, for the case in which prescribed external body director couples and director inertia are neglected. Details of the more general equations can be found in Rubin and Panteghini (2026).

The model consists of two interacting continua: a *macro*-continuum and a *micro*-continuum. The terms *macro* and *micro* are not used here in the sense of homogenization or representative volume element theory, and no volume-averaging procedure is involved. Rather, in the usual Cosserat sense, *macro* refers to the standard continuum, whereas *micro* refers to the additional director-based enriched response.

The macro-continuum governs the entire dissipative response and is described by a standard elastoplastic constitutive model. The micro-continuum is non-dissipative and contributes only through additional energetic terms associated with the mismatch between the directors $\mathbf{d}_i$ and material line elements $\mathbf{a}_i$, as well as through the corresponding director curvatures.

The two continua are constitutively uncoupled: the macro-response remains entirely standard, whereas the micro-response is governed by its own elastic energy. Their interaction is therefore not introduced through constitutive coupling terms, but arises from the kinematics together with the balance equations and boundary conditions.

This separation between macro- and micro-responses is a key feature of the formulation. All dissipation is confined to the macro-continuum, while the micro-continuum acts as an energetic mechanism that becomes relevant only when the deformation field develops sufficiently strong spatial variations. In this way, the model can influence localization patterns without modifying the standard elastoplastic constitutive structure of the macro-continuum.

2.1. Kinematics

With reference to Fig. 1, the kinematics is described in terms of a triad of vectors $\mathbf{a}_i$, representing material line elements, and a triad of directors $\mathbf{d}_i$, describing the micro-continuum. Under the assumption of small strains and rotations, the vectors $\mathbf{a}_i$ are obtained from the displacement gradient as

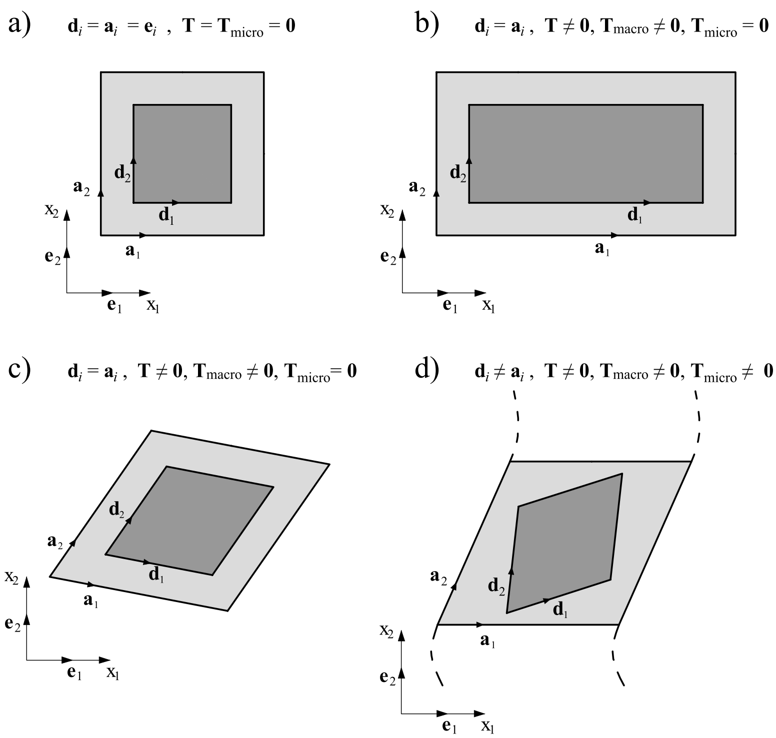

Fig. 1. Schematic representation of the kinematics of the deformable Cosserat model in a 2D setting. The vectors $\mathbf{a}_i$ denote the material line elements associated with the displacement gradient, whereas $\mathbf{d}_i$ denote the directors describing the micro-continuum. (a) Undeformed configuration, for which $\mathbf{d}_i = \mathbf{a}_i = \mathbf{e}_i$ and therefore $\mathbf{T} = \mathbf{T}_{\text{micro}} = \mathbf{0}$. (b) Homogeneous stretch: although $\mathbf{T} \neq \mathbf{0}$ and $\mathbf{T}_{\text{macro}} \neq \mathbf{0}$, the directors still follow the material line elements, so that $\mathbf{d}_i = \mathbf{a}_i$ and $\mathbf{T}_{\text{micro}} = \mathbf{0}$. (c) Homogeneous shear/distortion: again $\mathbf{d}_i = \mathbf{a}_i$, hence $\mathbf{T}_{\text{micro}} = \mathbf{0}$ and the response is entirely governed by the macro-continuum. (d) Non-homogeneous deformation: the directors no longer follow the material line elements, i.e. $\mathbf{d}_i \neq \mathbf{a}_i$, so that a mismatch develops and $\mathbf{T}_{\text{micro}} \neq \mathbf{0}$. The dashed lines schematically represent non-vanishing director curvatures, which generate corresponding micro-couples.

$$\mathbf{a}_i = \mathbf{e}_i + \left(\frac{\partial \mathbf{u}}{\partial \mathbf{x}}\right)\mathbf{e}_i \,, \tag{1}$$

where $\mathbf{u}$ is the displacement field and $\mathbf{e}_i$ is a fixed orthonormal triad.

The directors $\mathbf{d}_i$ are determined from a non-symmetric second-order tensor $\tilde{\boldsymbol{\eta}}$, as

$$\mathbf{d}_i = \mathbf{e}_i + \tilde{\boldsymbol{\eta}}^T \mathbf{e}_i \,. \tag{2}$$

With the curvature measure and the constitutive equation for the micro-couples adopted in this work, the skew-symmetric part of $\tilde{\boldsymbol{\eta}}$ is determined algebraically by the director momentum balance, as shown below. Consequently, in the reduced formulation used for the numerical implementation, only the symmetric part $\boldsymbol{\eta} = \text{sym}\,\tilde{\boldsymbol{\eta}}$ is retained as an independent primal kinematic field. Accordingly, each material point is characterized by 9 degrees of freedom in a general 3D setting (three displacement components and six components of $\boldsymbol{\eta}$), which reduce to 5 degrees of freedom in a 2D plane strain setting (two displacement components and three components of $\boldsymbol{\eta}$).

2.2. Balance laws and boundary conditions

In the quasi-static setting considered in this work, and in the absence of prescribed external body director couples, the balances of linear momentum and director momentum respectively read

$$\text{div}\,\mathbf{T} + \rho_0 \mathbf{b} = \mathbf{0} \,, \tag{3}$$

$$\mathbf{T}_{\text{micro}} + \text{div}\,\mathbf{M}^i \otimes \mathbf{e}_i = \mathbf{0} \,, \tag{4}$$

where $\mathbf{T}$ is the total stress tensor, $\mathbf{b}$ are the body forces (per unit mass), ρ_0 is the zero-stress density, $\mathbf{M}^i$ are second-order director couple tensors[1] having the dimensions of $[F][L]^{-1}$ and $\mathbf{T}_{\text{micro}}$ denotes the stress associated with the micro-continuum. The symmetry of $\mathbf{T}_{\text{micro}}$ and $\mathbf{T}$ for the present specialization follows from the skew-symmetric part of Eq. (4), as shown below. Here, $\text{div}(\cdot)$ is the divergence operator with respect to position $\mathbf{x}$, $\mathbf{a}\otimes\mathbf{b}$ denotes the tensor product between two vectors $\mathbf{a}$, $\mathbf{b}$, and the usual summation convention is used for repeated indices. The director momentum equation (4) determines the director field by relating the micro-stress to the divergence of the micro-couples. Since the micro-stress and the micro-couples are assumed to be linear elastic functions of χ and the director gradients, Eq. (4) is linear in the enhanced kinematic tensor $\tilde{\boldsymbol{\eta}}$ for a given displacement field. This property will play a key role in the simplicity of the resulting finite element formulation.

The traction vector $\mathbf{t}$ and the contact director couples $\boldsymbol{\mu}^i$, applied to a material surface ∂P with unit outward normal $\mathbf{n}$ are given by

$$\mathbf{t} = \mathbf{T}\cdot\mathbf{n}\,, \quad \boldsymbol{\mu}^i = \mathbf{M}^i\cdot\mathbf{n}\,, \tag{5}$$

so that their external power on ∂P is

$$\int_{\partial P} \left(\mathbf{t}\cdot\dot{\mathbf{u}} + \boldsymbol{\mu}^i\cdot\dot{\mathbf{d}}_i\right)\,\mathrm{d}S\,, \tag{6}$$

where $\mathrm{d}S$ is the element of area on ∂P.

2.3. Strain energy, rate of dissipation and constitutive equations

2.3.1. A general macro-continuum

Let Σ_{macro} be the specific (per unit mass) strain energy and $\mathbf{T}_{\text{macro}}$ be the stress tensor that characterize a general thermodynamically consistent small-deformation constitutive model for the macro-continuum. In particular, the macro-stress is symmetric,

$$\mathbf{T}^T_{\text{macro}} = \mathbf{T}_{\text{macro}}\,, \tag{7}$$

and the corresponding rate of material dissipation satisfies

$$\mathcal{D}_{\text{macro}} = \mathbf{T}_{\text{macro}} : \mathbf{D} - \rho_0\dot{\Sigma}_{\text{macro}} \geq 0\,, \tag{8}$$

where $\mathbf{D}$ is the symmetric part of the velocity gradient and ρ_0 is the constant density. The corresponding constitutive model may include elastic anisotropy and may depend on internal variables.

This macro-continuum can be enhanced using the deformable Cosserat model by adopting the specific strain energy Σ in the additive form

$$\Sigma = \Sigma_{\text{macro}} + \Sigma_{\text{micro}}\,, \tag{9}$$

and the total stress $\mathbf{T}$ in the additive form

$$\mathbf{T} = \mathbf{T}_{\text{macro}} + \mathbf{T}_{\text{micro}}\,, \tag{10}$$

with Σ_{micro} being the specific strain energy and $\mathbf{T}_{\text{micro}}$ the stress of the micro-continuum.

2.3.2. Micro-continuum energetics and model dissipation

As shown in Fig. 1, the micro-continuum stress $\mathbf{T}_{\text{micro}}$ is related to the *mismatch* between the directors $\mathbf{d}_i$ and material line elements described by $\mathbf{a}_i$, which is measured by the non-symmetric second-order tensor[2]

$$\chi = \partial\mathbf{u}/\partial\mathbf{x} - \tilde{\boldsymbol{\eta}}^T\,. \tag{11}$$

Thus, the micro-stress is driven by the tensor χ, which accounts for both relative deformation and relative rotation. In the present work, Σ_{micro} is specified as a quadratic form so that the micro-stress and micro-couples describe linear elastic response of $\mathbf{d}_i$ relative to $\mathbf{a}_i$.

The micro-curvature measure ζ^k_{ij} (which corresponds to the symbol χ^k_{ij} in Rubin and Panteghini (2026)) is introduced as

$$\zeta^k_{ij} = \left(\tilde{\eta}_{ij} + \tilde{\eta}_{ji}\right)_{,k}\,, \tag{12}$$

where $(\cdot)_{,k}$ denotes partial differentiation with respect to the kth spatial coordinate x_k. The superscript k in ζ^k_{ij} is retained only to follow the notation of Rubin and Panteghini (2026); it labels the Cartesian direction of differentiation, namely the same index appearing after the comma, and does not denote a contravariant component. In this paper, the strain energy density of the micro-continuum is taken as:

[1] Following Rubin and Panteghini (2026), the superscript in $\mathbf{M}^i$ labels the director to which the couple tensor is associated and does not denote a contravariant component. All component expressions are written with respect to the fixed Cartesian basis used throughout this work; hence no distinction between covariant and contravariant components is made. In this notation, $\mathbf{M}^i = M^i_{jk}\mathbf{e}_j\otimes\mathbf{e}_k$. In component form, i, j, and k are Cartesian component indices, with i identifying the associated director and j,k denoting the components of the corresponding second-order couple tensor.

[2] Using the definition of χ^j_i of Rubin and Panteghini (2026), $\chi = \chi^j_i\,\mathbf{e}_j\otimes\mathbf{e}_i$

$$\rho_0 \Sigma_{\text{micro}} = \frac{G}{2} \left\{ k_1 (\chi : \mathbf{I})^2 + k_2 \chi' : \chi' + \ell^2 \zeta^k_{ij} \zeta^k_{ij} \right\}, \tag{13}$$

where $G > 0$ is the shear modulus, k_1 and k_2 are non-negative dimensionless material constants, and ℓ is a constitutive material length-scale parameter. Moreover, $(\cdot)'$ denotes the deviatoric part of a second-order tensor and $:$ denotes the inner product between two second-order tensors.

Consistently with the small-strain framework adopted here and following (Rubin & Panteghini, 2026), the rate of dissipation of the deformable Cosserat model can be written as

$$\mathcal{D} = \mathbf{T} : \mathbf{L} - \mathbf{T}_{\text{micro}} : \dot{\tilde{\boldsymbol{\eta}}}^T + M^i_{jk} \dot{\tilde{\eta}}_{ij,k} - \rho_0 \dot{\Sigma} \geq 0, \tag{14}$$

where $\mathbf{L} = \partial \dot{\mathbf{u}} / \partial \mathbf{x}$ is the velocity gradient. By considering the stress decomposition (10), recalling that $\mathbf{T}_{\text{macro}}$ is symmetric, and using the definition of χ given in Eq. (11), the rate of dissipation can be rewritten as

$$\mathcal{D} = \mathbf{T}_{\text{macro}} : \mathbf{D} + \mathbf{T}_{\text{micro}} : \dot{\chi} + M^i_{jk} \dot{\tilde{\eta}}_{ij,k} - \rho_0 \dot{\Sigma} \geq 0. \tag{15}$$

Since the constitutive response of the micro-continuum is taken to be purely energetic (and hence non-dissipative), its mechanical power is exactly balanced by the rate of the micro-strain energy:

$$\mathbf{T}_{\text{micro}} : \dot{\chi} + M^i_{jk} \dot{\tilde{\eta}}_{ij,k} - \rho_0 \dot{\Sigma}_{\text{micro}} = 0, \tag{16}$$

for all deformation processes. It follows that the micro-stress $\mathbf{T}_{\text{micro}}$ and the micro-couples M^i_{jk} are given by

$$\begin{aligned} \mathbf{T}_{\text{micro}} &= \rho_0 \frac{\partial \Sigma_{\text{micro}}}{\partial \chi} = G \left(k_1 \mathbf{I} \otimes \mathbf{I} + k_2 \mathcal{I}_d \right) \chi, \\ M^i_{jk} &= \rho_0 \frac{\partial \Sigma_{\text{micro}}}{\partial \tilde{\eta}_{ij,k}} = 2G\ell^2 \zeta^k_{ij}, \end{aligned} \tag{17}$$

where $\mathcal{I}_d = \mathcal{I} - (1/3)\mathbf{I} \otimes \mathbf{I}$ is the deviatoric projection operator, with $\mathcal{I}$ denoting the fourth-order identity tensor. Then, with the help of Eq. (16), the rate of dissipation (15) requires

$$\mathcal{D} = \mathcal{D}_{\text{macro}} \geq 0. \tag{18}$$

This proves that all material dissipation in the present deformable Cosserat model is due to the macro-continuum, whereas the micro-continuum contributes only through energetic terms.

2.3.3. Coupling of the macro- and micro-continua

The *constitutive* equations of the micro-continuum are uncoupled from those of the macro-continuum. Specifically, for a given displacement gradient $\partial \mathbf{u} / \partial \mathbf{x}$, the relative elastic measure χ in Eq. (11), the curvature measure ζ^k_{ij} in Eq. (12), and the corresponding micro-stress $\mathbf{T}_{\text{micro}}$ and micro-couples M^i_{jk} in Eq. (17) are determined by the director field $\tilde{\boldsymbol{\eta}}$ through the director momentum equation and the associated boundary conditions.

Although the constitutive response of the micro-continuum is uncoupled from that of the macro-continuum, the response of the deformable Cosserat model is coupled. Specifically, the total stress $\mathbf{T}$ entering the balance of linear momentum and the traction boundary conditions contains the contribution of the micro-stress through Eq. (10). In this way, the interaction between macro- and micro-response is introduced through the kinematics, the balance equations, and the boundary conditions, rather than through direct constitutive coupling terms.

2.3.4. Specific macro-constitutive equations used in the present paper

From the standpoint of thermodynamic consistency and of the black-box macro-stress update, the framework introduced above requires the macro-continuum to be described by a thermodynamically consistent small-strain dissipative constitutive model.

In the macro-continuum, the stress $\mathbf{T}_{\text{macro}}$ is assumed to depend on the *symmetric* elastic strain $\boldsymbol{\varepsilon}_e$. Its evolution is governed by

$$\dot{\boldsymbol{\varepsilon}}_e = \mathbf{D} - \mathbf{D}_p, \tag{19}$$

where $\mathbf{D}$ is the symmetric part of the velocity gradient and $\mathbf{D}_p$ is the symmetric rate of plastic deformation of the macro-continuum. This relation has the standard physical meaning of infinitesimal elastoplasticity: the elastic strain of the macro-continuum evolves with the total symmetric rate of deformation, while the rate of plastic deformation accounts for the dissipative part of the macro-response. Accordingly, the macro-stress is determined by $\boldsymbol{\varepsilon}_e$, whereas dissipation is associated with $\mathbf{D}_p$.

This form of constitutive description is consistent with Eulerian formulations of elastoplasticity. As already recognized by Eckart (1948) and later developed by Leonov (1976), stress can be characterized through the evolution of an elastic deformation measure rather than through an explicit decomposition based on reference or intermediate configurations. In the present small-deformation setting, this measure is the symmetric elastic strain $\boldsymbol{\varepsilon}_e$ governed by Eq. (19).

Moreover, the specific strain energy function $\Sigma_{\text{macro}}(\boldsymbol{\varepsilon}_e)$ is taken to be a function of the elastic strain $\boldsymbol{\varepsilon}_e$ only with the macro-stress given by

$$\mathbf{T}_{\text{macro}} = \rho_0 \frac{\partial \Sigma_{\text{macro}}}{\partial \boldsymbol{\varepsilon}_e}. \tag{20}$$

Also, $\mathbf{D}_p$ is determined by an associated flow rule using a specified convex yield function, so that the rate of dissipation (18) becomes

$$\mathcal{D} = \mathcal{D}_{\text{macro}} = \mathbf{T}_{\text{macro}} : \mathbf{D}_p \geq 0\,, \tag{21}$$

which is satisfied automatically.

2.4. Consequences of the chosen curvature measure

The reduction to the symmetric director field follows from the structure of the curvature measure adopted in this work. From Eqs. (12) and (17), the director couple tensors are

$$M^i_{jk} = 2G\ell^2 \left(\tilde{\eta}_{ij} + \tilde{\eta}_{ji}\right)_{,k}\,. \tag{22}$$

Therefore, the divergence term entering the director momentum balance has components

$$\left(\operatorname{div}\mathbf{M}^i \otimes \mathbf{e}_i\right)_{ji} = M^i_{jk,k} = 2G\ell^2 \left(\tilde{\eta}_{ij} + \tilde{\eta}_{ji}\right)_{,kk}\,. \tag{23}$$

This tensor is symmetric. Hence, the skew-symmetric part of the director momentum balance does not contain curvature terms and does not provide a differential equation for the skew-symmetric part of $\tilde{\boldsymbol{\eta}}$.

Let

$$\tilde{\boldsymbol{\eta}} = \boldsymbol{\eta} + \boldsymbol{\eta}_\Omega, \qquad \boldsymbol{\eta} = \operatorname{sym}\tilde{\boldsymbol{\eta}}, \qquad \boldsymbol{\eta}_\Omega = \operatorname{skw}\tilde{\boldsymbol{\eta}}, \tag{24}$$

and decompose the displacement gradient as

$$\frac{\partial \mathbf{u}}{\partial \mathbf{x}} = \boldsymbol{\varepsilon} + \boldsymbol{\Omega}, \qquad \boldsymbol{\varepsilon} = \operatorname{sym}\frac{\partial \mathbf{u}}{\partial \mathbf{x}}, \qquad \boldsymbol{\Omega} = \operatorname{skw}\frac{\partial \mathbf{u}}{\partial \mathbf{x}}. \tag{25}$$

Using $\chi = \partial\mathbf{u}/\partial\mathbf{x} - \tilde{\boldsymbol{\eta}}^T$, one obtains

$$\chi_{\text{sym}} = \boldsymbol{\varepsilon} - \boldsymbol{\eta}, \qquad \chi_{\text{skw}} = \boldsymbol{\Omega} + \boldsymbol{\eta}_\Omega. \tag{26}$$

Since the spherical part of the micro-stress does not act on skew-symmetric tensors, the skew-symmetric part of the micro-stress is

$$\left(\mathbf{T}_{\text{micro}}\right)_{\text{skw}} = Gk_2\,\chi_{\text{skw}}. \tag{27}$$

For the specialization considered in this work, external body micro-couples and director inertia are neglected. The skew-symmetric part of Eq. (4) therefore reduces to

$$Gk_2\,\chi_{\text{skw}} = \mathbf{0}. \tag{28}$$

Thus, for $k_2 > 0$,

$$\chi_{\text{skw}} = \mathbf{0}, \qquad \boldsymbol{\eta}_\Omega = -\boldsymbol{\Omega}. \tag{29}$$

The skew-symmetric part of $\tilde{\boldsymbol{\eta}}$ is therefore determined algebraically by the skew-symmetric part of the displacement gradient. Hence, it is not retained as an independent primal kinematic field in the formulation used in the numerical implementation. The retained director field is the symmetric tensor $\boldsymbol{\eta} = \operatorname{sym}\tilde{\boldsymbol{\eta}}$. Consequently,

$$\chi = \boldsymbol{\varepsilon} - \boldsymbol{\eta} = \chi^T, \qquad \zeta^k_{ij} = 2\eta_{ij,k}. \tag{30}$$

Under the same assumptions, $\mathbf{T}_{\text{micro}}$ is symmetric. Since the macro-stress $\mathbf{T}_{\text{macro}}$ is symmetric, the total stress $\mathbf{T} = \mathbf{T}_{\text{macro}} + \mathbf{T}_{\text{micro}}$ is symmetric as well. In the more general theory, body micro-couples or director inertia would enter the skew-symmetric director balance as additional source terms; the corresponding details are given in the companion paper (Rubin & Panteghini, 2026).

3. Finite element formulation

The internal virtual power δW^{int} of a continuum occupying a region P is expressed as[3]

$$\delta W^{\text{int}} = \int_P \left[T_{ij}\delta\varepsilon_{ij} - \left(\mathbf{T}_{\text{micro}}\right)_{ij}\delta\eta_{ij} + M^i_{jk}\delta\eta_{ij,k}\right] \mathrm{d}V\,, \tag{31}$$

where $\delta\mathbf{u}$ and $\delta\boldsymbol{\eta}$ denote arbitrary kinematically admissible variations, with $\delta\boldsymbol{\eta} = \delta\boldsymbol{\eta}^T$. Moreover, $\delta\epsilon$ is the symmetric strain variation associated with $\delta\mathbf{u}$, i.e.,

$$\delta\varepsilon_{ij} = \frac{1}{2}\left(\delta u_{i,j} + \delta u_{j,i}\right),$$

[3] It should be noted that Eq. (31) is a special case, for the simple *constitutive* assumptions adopted here and in the absence of external director couples and director inertia. For a more general expression, the reader is referred to Rubin and Panteghini (2026).

and $\mathrm{d}V$ is the volume element.

The adopted FE discretization is isoparametric, such that the same shape functions are employed to interpolate both the reference geometry and the displacement field, i.e.

$$x_j(\boldsymbol{r}) = \sum_{k=1}^{n} N^{(k)}(\boldsymbol{r})\hat{x}_j^{(k)}, \quad u_j(\boldsymbol{r}) = \sum_{k=1}^{n} N^{(k)}(\boldsymbol{r})\hat{u}_j^{(k)},$$

where x_j and u_j are the jth components of the coordinates and of the displacement, respectively, n is the total number of nodes, $N^{(k)}(\boldsymbol{r})$ is a standard polynomial shape function referred to the kth node, $\boldsymbol{r}$ is the vector containing the intrinsic coordinates of the parent element, and $\hat{x}_j^{(k)}$ and $\hat{u}_j^{(k)}$ are, respectively, the jth coordinate and the jth displacement component of the kth node.[4]

Since the micro-distortion tensor $\boldsymbol{\eta}$ is symmetric, only its independent components are retained as primary variables. These components are interpolated through the shape functions $N_\eta^{(k)}(\boldsymbol{r})$ and collected, at the element level, in the nodal vector $\hat{\boldsymbol{\eta}}$. Accordingly, the interpolated micro-distortion field can be written in array notation as

$$\boldsymbol{\eta} = \mathcal{N}_\eta \hat{\boldsymbol{\eta}}, \tag{32}$$

where $\mathcal{N}_\eta = \mathcal{N}_\eta(\mathbf{N}_\eta)$ is the FE interpolation operator[5] associated with the micro-distortion field.

The number of nodes used for the interpolation of $\boldsymbol{\eta}$ is denoted by $n_\eta \leq n$. The shape functions $N_\eta^{(k)}(\boldsymbol{r})$, collected in the vector $\mathbf{N}_\eta$, may be of different order with respect to the displacement shape functions $N^{(k)}(\boldsymbol{r})$.

The matrices $\mathbf{H}$ and $\mathbf{H}_\eta$, respectively containing the derivatives of the shape functions $N^{(k)}$ and $N_\eta^{(k)}$ with respect to the coordinate system, can be computed as

$$\mathbf{H} = \boldsymbol{J}^{-1}\mathbf{H}_r, \quad \mathbf{H}_\eta = \boldsymbol{J}^{-1}\mathbf{H}_{\eta r}, \quad \boldsymbol{J} = \mathbf{H}_r\hat{\mathbf{X}}, \tag{33}$$

where $\mathbf{H}_r$ and $\mathbf{H}_{\eta r}$ are, respectively, the matrices that contain the derivatives of the shape functions $N^{(k)}$ and $N_\eta^{(k)}$ with respect to $\boldsymbol{r}$ and $\boldsymbol{J}$ is the Jacobian matrix, and $\hat{\mathbf{X}}$ is a matrix containing the nodal coordinates.

By adopting an array notation[6] the fields $\delta\varepsilon_{ij}$, $\delta\eta_{ij}$ and $\delta\eta_{ij,k}$ can be discretized as functions of the nodal variations $\delta\hat{\mathbf{u}}$ and $\delta\hat{\boldsymbol{\eta}}$ as:

$$\delta\varepsilon = \mathcal{B}\,\delta\hat{\mathbf{u}}, \quad \delta\boldsymbol{\eta} = \mathcal{N}_\eta\delta\hat{\boldsymbol{\eta}}, \quad \delta\boldsymbol{\eta}_{,k} = \mathcal{G}_\eta\delta\hat{\boldsymbol{\eta}}, \tag{34}$$

where $\mathcal{B} = \mathcal{B}(\mathbf{H})$, and $\mathcal{G}_\eta = \mathcal{G}_\eta(\mathbf{H}_\eta)$ are FE operators.

Under these assumptions, the internal virtual power (31) can be discretized as

$$\delta W^{\text{int}} = \int_P \left[\delta\hat{\mathbf{u}}^T\mathcal{B}^T\mathbf{T} + \delta\hat{\boldsymbol{\eta}}^T\left(\mathcal{G}_\eta^T\mathbf{M} - \mathcal{N}_\eta^T\mathbf{T}_{\text{micro}}\right)\right]\mathrm{d}V, \tag{35}$$

which, being valid for any kinematically admissible value of $\delta\hat{\mathbf{u}}, \delta\hat{\boldsymbol{\eta}}$, gives the following internal forces:

$$\mathbf{F}_{\text{u}}^{\text{int}} = \int_P \mathcal{B}^T\mathbf{T}\,\mathrm{d}V, \quad \mathbf{F}_\eta^{\text{int}} = \int_P \left(\mathcal{G}_\eta^T\mathbf{M} - \mathcal{N}_\eta^T\mathbf{T}_{\text{micro}}\right)\mathrm{d}V. \tag{36}$$

The non-standard micro-stress $\mathbf{T}_{\text{micro}}$ and the micro-couples M^i_{jk}, here collected in the vector $\mathbf{M}$, are computed directly from the nodal variables through the linear elastic relations of the micro-continuum. In particular, considering that χ is a symmetric tensor, from Eq. (17) and (26) it follows that:

$$\begin{aligned}\mathbf{T}_{\text{micro}} &= G\left(k_1\mathbf{I}\otimes\mathbf{I} + k_2\,\mathcal{I}^v_{\text{dev}}\right)\left(\mathcal{B}\,\hat{\mathbf{u}} - \mathcal{N}_\eta\,\hat{\boldsymbol{\eta}}\right), \\ M^i_{jk} &= 4G\ell^2\eta_{ij,k} \to \mathbf{M} = 4G\ell^2\,\mathcal{G}_\eta\,\hat{\boldsymbol{\eta}},\end{aligned} \tag{37}$$

---

[4] In this work the hat symbol, $(\hat{\cdot})$ denotes the nodal values of the corresponding variables.

[5] All the FE operators are reported in Appendix for 2D plane strain.

[6] In this footnote, square brackets denote the tensor or matrix representation of a quantity before it is collected into the corresponding array used in the finite element implementation. For the 2D plane strain implementation, the symmetric stress and strain-like quantities are stored in four-component arrays. Stress-like arrays contain the physical shear stress, whereas strain-like arrays contain the engineering shear component. For instance,

$$[\mathbf{T}] = \begin{bmatrix} T_{11} & T_{12} & 0 \\ T_{12} & T_{22} & 0 \\ 0 & 0 & T_{33} \end{bmatrix} \to \mathbf{T} = \begin{bmatrix} T_{11} \\ T_{22} \\ T_{33} \\ T_{12} \end{bmatrix}, \qquad \varepsilon = \begin{bmatrix} \varepsilon_{11} \\ \varepsilon_{22} \\ 0 \\ 2\varepsilon_{12} \end{bmatrix}, \quad \boldsymbol{\eta} = \begin{bmatrix} \eta_{11} \\ \eta_{22} \\ 0 \\ 2\eta_{12} \end{bmatrix}.$$

Moreover, the tensorial gradients of the symmetric micro-distortion and the corresponding micro-couples are stored as:

$$[\eta_{ij,k}] \to \boldsymbol{\eta}_{,k} = \begin{bmatrix} \eta_{11,1} \\ \eta_{22,1} \\ \eta_{12,1} \\ \eta_{21,1} \\ \eta_{11,2} \\ \eta_{22,2} \\ \eta_{12,2} \\ \eta_{21,2} \end{bmatrix}, \quad [M^i_{jk}] \to \mathbf{M} = \begin{bmatrix} M^1_{11} \\ M^2_{21} \\ M^1_{21} \\ M^2_{11} \\ M^1_{12} \\ M^2_{22} \\ M^1_{22} \\ M^2_{12} \end{bmatrix}, \qquad \eta_{12,k} = \eta_{21,k}.$$

where $\mathcal{I}^{v}_{\text{dev}}$ denotes the deviatoric projection written in the Voigt notation. The macro-stress $\mathbf{T}_{\text{macro}}$ is the only part affected by elastoplasticity. It is a symmetric stress that depends on the symmetric elastic strain of the macro-continuum, on the increment of the symmetric part of the displacement gradient,

$$\Delta\boldsymbol{\varepsilon}_{\text{macro}} = \mathcal{B}\,\Delta\hat{\mathbf{u}}\,, \tag{38}$$

and on a set of internal variables $\mathbf{p}_{\text{macro}}$ associated exclusively with the standard plastic response.

Accordingly, the macro stress $\mathbf{T}_{\text{macro}}$ is obtained from a standard elastoplastic constitutive update as:

$$\mathbf{T}_{\text{macro}} = \mathbf{T}_{\text{macro}}\big(\Delta\boldsymbol{\varepsilon}_{\text{macro}},\, \boldsymbol{\varepsilon}^{\text{e}}_{\text{macro},n},\, \mathbf{p}_{\text{macro}}\big), \tag{39}$$

where $\boldsymbol{\varepsilon}^{\text{e}}_{\text{macro},n}$ are the (standard) elastic strains of the macro-continuum at the beginning of the increment, i.e., at time t_n. This is the central feature of the formulation: both the macro-stress and the corresponding local material consistent elastoplastic tangent can be obtained directly from *any* standard elastoplastic constitutive routine, which can therefore be employed as a black box without modifying either the local stress-update algorithm or the local material tangent operator. Hence, the stress $\mathbf{T}$ can be computed from Eq. (10) as:

$$\mathbf{T} = \mathbf{T}_{\text{macro}} + G\left(k_1\mathbf{I}\otimes\mathbf{I} + k_2\,\mathcal{I}^{v}_{\text{dev}}\right)\left(\mathcal{B}\,\hat{\mathbf{u}} - \mathcal{N}_{\eta}\,\hat{\boldsymbol{\eta}}\right). \tag{40}$$

The FE stiffness matrix is obtained by differentiating the internal forces $\mathbf{F}^{\text{int}}_{\text{u}}$ and $\mathbf{F}^{\text{int}}_{\eta}$ with respect to the nodal displacements $\hat{\mathbf{u}}$ and the nodal tensor $\hat{\boldsymbol{\eta}}$, i.e.,

$$\mathbf{K} = \begin{bmatrix} \mathbf{K}_{\text{uu}} & \mathbf{K}_{\text{u}\eta} \\ \mathbf{K}_{\eta\text{u}} & \mathbf{K}_{\eta\eta} \end{bmatrix} \tag{41}$$

where:

$$\mathbf{K}_{\text{uu}} = \int_P \mathcal{B}^T\left[\frac{\partial\mathbf{T}_{\text{macro}}}{\partial\boldsymbol{\varepsilon}_{\text{macro}}} + G\left(k_1\mathbf{I}\otimes\mathbf{I} + k_2\,\mathcal{I}^{v}_{\text{dev}}\right)\right]\mathcal{B}\,\mathrm{d}V\,, \tag{42}$$

$$\mathbf{K}_{\text{u}\eta} = \int_P -G\mathcal{B}^T\left(k_1\mathbf{I}\otimes\mathbf{I} + k_2\,\mathcal{I}^{v}_{\text{dev}}\right)\mathcal{N}_{\eta}\,\mathrm{d}V\,, \tag{43}$$

$$\mathbf{K}_{\eta\text{u}} = \int_P -G\,\mathcal{N}^T_{\eta}\left(k_1\mathbf{I}\otimes\mathbf{I} + k_2\,\mathcal{I}^{v}_{\text{dev}}\right)\mathcal{B}\,\mathrm{d}V\,, \tag{44}$$

$$\mathbf{K}_{\eta\eta} = \int_P G\left[\mathcal{N}^T_{\eta}\left(k_1\mathbf{I}\otimes\mathbf{I} + k_2\,\mathcal{I}^{v}_{\text{dev}}\right)\mathcal{N}_{\eta} + 4\ell^2\left(\mathcal{G}^T_{\eta}\,\mathcal{G}_{\eta}\right)\right]\mathrm{d}V\,. \tag{45}$$

It is worth noting that, if the material consistent elastoplastic tangent $\partial\mathbf{T}_{\text{macro}}/\partial\boldsymbol{\varepsilon}_{\text{macro}}$ of the standard macro-continuum is symmetric, then the resulting FE stiffness matrix $\mathbf{K}$ is also symmetric.

It should be noted that, once $\mathbf{T}_{\text{macro}}$ and the local material consistent elastoplastic tangent $\partial\mathbf{T}_{\text{macro}}/\partial\boldsymbol{\varepsilon}_{\text{macro}}$ are obtained from a standard constitutive update, the entire formulation reduces to the assembly of the additional linear contributions associated with the micro-continuum. The complete FE algorithm is summarized in Algorithm 1.

4. Benchmark problem: shallow strip footing

A shallow rigid strip footing has been analyzed under plane strain conditions by employing either the Tresca or the Matsuoka–Nakai (Matsuoka & Nakai, 1974; Panteghini & Lagioia, 2014) plasticity models. Whilst the former is typically adopted to reproduce the behavior of soils in undrained conditions, the latter class of models is more appropriate for frictional geomaterials in drained regimes.

The considered benchmark is well known to be particularly demanding from a numerical standpoint (de Borst & Vermeer, 1984), as it involves the development of highly localized deformation patterns beneath the footing, often associated with the interaction of multiple failure mechanisms. Such features make it especially suitable for assessing the ability of a numerical formulation to capture strain localization in a mesh-objective manner.

The footing has a total width $2B = 2\,\text{m}$ and is subjected to vertical and centered loading conditions. The out-of-plane thickness h is equal to $1\,\text{m}$. Owing to symmetry, only half of the domain is modeled, corresponding to a footing width $B = 1\,\text{m}$. The soil domain extends over a $50\,\text{m} \times 50\,\text{m}$ region, which is sufficiently large to avoid any spurious influence of the boundary conditions on the computed response.

Boundary conditions, schematically reported in Fig. 2, are prescribed as follows. Along the axis of symmetry, the horizontal displacement is constrained, $u_1 = 0$, and the off-diagonal component of the symmetric director field is set equal to zero, $\eta_{12} = 0$, consistently with symmetry. No other essential boundary conditions are imposed on $\boldsymbol{\eta}$; hence, on the remaining boundaries, the additional kinematic degrees of freedom are left free and the corresponding natural condition is a vanishing contact director couple. Along the right boundary, only the horizontal displacement is constrained, whereas along the bottom boundary only the vertical displacement is constrained. The rigid strip footing is modeled by prescribing the vertical displacement of the soil nodes located beneath the footing. The horizontal displacement of the same nodes is also constrained, $u_1 = 0$, so as to prevent tangential relative motion between the soil and the footing.

Algorithm 1 Algorithm for the FE formulation

At the element level, the formulation is expressed in terms of the nodal variables $\hat{\mathbf{u}}$ and $\hat{\boldsymbol{\eta}}$, together with the standard constitutive variables of the macro-continuum at the beginning of the increment.

ASSEMBLE the FE operators $\mathcal{B}$, $\mathcal{N}_\eta$, and $\mathcal{G}_\eta$ from the shape functions and their derivatives;

COMPUTE the macro (standard) strain increment $\Delta\boldsymbol{\epsilon}_{\mathrm{macro}}$ from the nodal displacement increment using Eq. (38):

$$\Delta\boldsymbol{\epsilon}_{\mathrm{macro}} = \mathcal{B}\Delta\hat{\mathbf{u}}\,;$$

CALL the standard elastoplastic routine to compute the response of the macro-continuum:

GIVEN

the (standard) elastic strain $\boldsymbol{\epsilon}^{\mathrm{e}}_{\mathrm{macro},n}$ (at the beginning of the increment, i.e., at time t_n),

the (standard) state variables $\mathbf{p}_{\mathrm{macro},n}$ (at the beginning of the increment, i.e., at time t_n),

the macro strain increment $\Delta\boldsymbol{\epsilon}_{\mathrm{macro}}$,

COMPUTE

the (standard) macro-stress $\mathbf{T}_{\mathrm{macro}}$,

the (standard) elastic strain of the macro-continuum $\boldsymbol{\epsilon}^{\mathrm{e}}_{\mathrm{macro}}$,

the (standard) local material consistent elastoplastic tangent $\partial\mathbf{T}_{\mathrm{macro}}/\partial\boldsymbol{\epsilon}_{\mathrm{macro}}$,

the updated (standard) state variables $\mathbf{p}_{\mathrm{macro}}$ of the macro-continuum.

COMPUTE the (symmetric) micro stress $\mathbf{T}_{\mathrm{micro}}$ and the micro-couples $\mathbf{M}$ using Eq. (37):

$$\mathbf{T}_{\mathrm{micro}} = G\left(k_1\mathbf{I}\otimes\mathbf{I} + k_2\,\mathcal{I}^{v}_{\mathrm{dev}}\right)\left(\mathcal{B}\hat{\mathbf{u}} - \mathcal{N}_\eta\hat{\boldsymbol{\eta}}\right), \quad \mathbf{M} = 4G\ell^2\,\mathcal{G}_\eta\,\hat{\boldsymbol{\eta}}\,;$$

COMPUTE the internal forces $\mathbf{F}^{\mathrm{int}}_{\mathrm{u}}$ and $\mathbf{F}^{\mathrm{int}}_{\eta}$ using Eq. (36):

$$\mathbf{F}^{\mathrm{int}}_{\mathrm{u}} = \int_P \mathcal{B}^T\left(\mathbf{T}_{\mathrm{macro}} + \mathbf{T}_{\mathrm{micro}}\right)\,\mathrm{d}V\,, \quad \mathbf{F}^{\mathrm{int}}_{\eta} = \int_P \left(\mathcal{G}_\eta{}^T\mathbf{M} - \mathcal{N}_\eta{}^T\mathbf{T}_{\mathrm{micro}}\right)\mathrm{d}V\,;$$

COMPUTE the FE stiffness matrix $\mathbf{K}$ using Eqs. (41)–(45):

$$\mathbf{K} = \begin{bmatrix}\mathbf{K}_{\mathrm{uu}} & \mathbf{K}_{\mathrm{u}\eta}\\ \mathbf{K}_{\eta\mathrm{u}} & \mathbf{K}_{\eta\eta}\end{bmatrix}\,,$$

where:

$$\mathbf{K}_{\mathrm{uu}} = \int_P \mathcal{B}^T\left[\frac{\partial\mathbf{T}_{\mathrm{macro}}}{\partial\boldsymbol{\epsilon}_{\mathrm{macro}}} + G\left(k_1\mathbf{I}\otimes\mathbf{I} + k_2\,\mathcal{I}^{v}_{\mathrm{dev}}\right)\right]\mathcal{B}\,\mathrm{d}V\,, \quad \mathbf{K}_{\mathrm{u}\eta} = \int_P -G\mathcal{B}^T\left(k_1\mathbf{I}\otimes\mathbf{I} + k_2\,\mathcal{I}^{v}_{\mathrm{dev}}\right)\mathcal{N}_\eta\,\mathrm{d}V\,,$$

$$\mathbf{K}_{\eta\mathrm{u}} = \int_P -G\,\mathcal{N}^T_\eta\left(k_1\mathbf{I}\otimes\mathbf{I} + k_2\,\mathcal{I}^{v}_{\mathrm{dev}}\right)\mathcal{B}\,\mathrm{d}V\,, \quad \mathbf{K}_{\eta\eta} = \int_P G\left[\mathcal{N}^T_\eta\left(k_1\mathbf{I}\otimes\mathbf{I} + k_2\,\mathcal{I}^{v}_{\mathrm{dev}}\right)\mathcal{N}_\eta + 4\ell^2\left(\mathcal{G}^T_\eta\,\mathcal{G}_\eta\right)\right]\mathrm{d}V\,.$$

The above algorithm is written in a compact operator form and is also valid for the fully three-dimensional formulation once the corresponding three-dimensional FE operators are introduced. The FE operators $\mathcal{B}$, $\mathcal{N}_\eta$, and $\mathcal{G}_\eta$ are detailed in Appendix for the 2D plane strain case.

Depending on the constitutive model and loading scenario, the analyses are performed either starting from an unstressed initial configuration or from an initial geostatic state induced by self-weight. The latter case is particularly relevant for frictional soils, where the stress field generated by gravity plays a crucial role in the subsequent development of failure mechanisms. The specific assumptions adopted in each case are detailed in the following subsections.

The mechanical behavior of the macro-continuum is described by an isotropic elastoplastic model with linear elasticity and associated plasticity, based on the General Yield Criterion proposed by Lagioia and Panteghini (2016). The yield function is expressed as

$$f = q\,\Gamma_f(\theta) - M(\bar{\varepsilon}_p)\,p - \kappa(\bar{\varepsilon}_p), \tag{46}$$

where $q = \sqrt{\frac{3}{2}\mathbf{T}'_{\mathrm{macro}} : \mathbf{T}'_{\mathrm{macro}}}$ denotes the equivalent von Mises macro-stress, $p = -(\mathbf{T}_{\mathrm{macro}} : \mathbf{I})/3$ is the mean macro-stress, and

$$\theta = \frac{1}{3}\arcsin\left(-\frac{27}{2}\frac{\det\mathbf{T}'_{\mathrm{macro}}}{q^3}\right) \tag{47}$$

is the Lode angle. The scalar variable $\bar{\varepsilon}_p$ represents a measure of accumulated plastic strain.

The function $\Gamma_f(\theta)$ controls the shape of the yield surface in the octahedral plane and is defined as

$$\Gamma_f(\theta) = a_f\cos\left[\frac{\arccos\left(-b_f\sin 3\theta\right)}{3} - c_f\frac{\pi}{6}\right]. \tag{48}$$

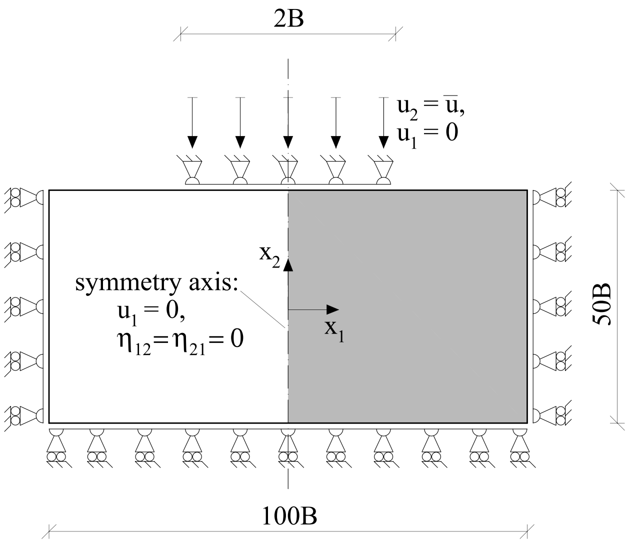

Fig. 2. Geometry (not to scale) and boundary conditions for the footing benchmark. Due to symmetry, only a half of the domain, shown gray, has been simulated. The footing is subjected to a prescribed vertical displacement $\bar{u}$ and zero horizontal displacement. The vertical dashed line denotes the symmetry axis.

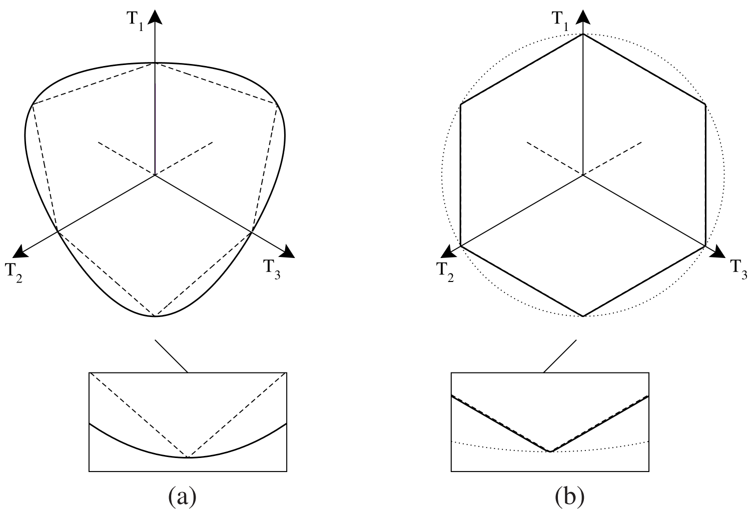

Fig. 3. Plot of the adopted yield criteria in the octahedral plane. (a) The solid line is the Matsuoka–Nakai criterion. For comparison the dashed line is the Mohr–Coulomb yield criterion for the same shear resistance angle $\phi = 20°$; (b) The solid line is the Rounded Tresca criterion based on the parameters reported in Table 1. For comparison the dashed line is the sharp Tresca criterion and the dotted line is the von Mises circle.

By appropriate selection of the parameters a_f, b_f, and c_f, this formulation can reproduce a variety of classical yield criteria, including rounded Tresca and Matsuoka–Nakai (Matsuoka & Nakai, 1974; Panteghini & Lagioia, 2014), as well as Lade and Duncan (1974) and von Mises.

In the case of criteria exhibiting corners in the octahedral plane, the adopted parameters smooth the apexes while preserving convexity of the yield surface. In the present study, the shape of the octahedral section is kept constant throughout the analysis, i.e. the parameters a_f, b_f, and c_f do not evolve with plastic deformation. The values adopted to reproduce the rounded Tresca and Matsuoka–Nakai criteria are reported in Table 1, and the corresponding shape functions are shown in Fig. 3.

The material parameter $M(\bar{\varepsilon}_p)$, defined as a function of the shear resistance angle ϕ as

$$M(\bar{\varepsilon}_p) = \frac{6 \sin\phi(\bar{\varepsilon}_p)}{3 - \sin\phi(\bar{\varepsilon}_p)}\,, \tag{49}$$

Table 1
Material parameters adopted for the shape function Γ_f, with ϕ being the shear resistance angle.

Model	a_f	b_f	c_f
Outer smooth Tresca	1.151579	0.9999	1.0
Matsuoka–Nakai, $\phi = 30°$	1.442221	0.746712	0.0
Matsuoka–Nakai, $\phi = 20°$	1.328450	0.552093	0.0

Table 2
Meshes for the strip footing problem.

Mesh	Number of Elements	Number of Nodes	Characteristic Element Length ℓ_e	DoFs
1	7916	24,028	$13.4 \cdot 10^{-2}$ m	72,222
2	31,664	95,550	$6.715 \cdot 10^{-2}$ m	286,927
3	126,656	381,082	$3.358 \cdot 10^{-2}$ m	1,143,801
4	506,624	1,522,098	$1.679 \cdot 10^{-2}$ m	4,567,405

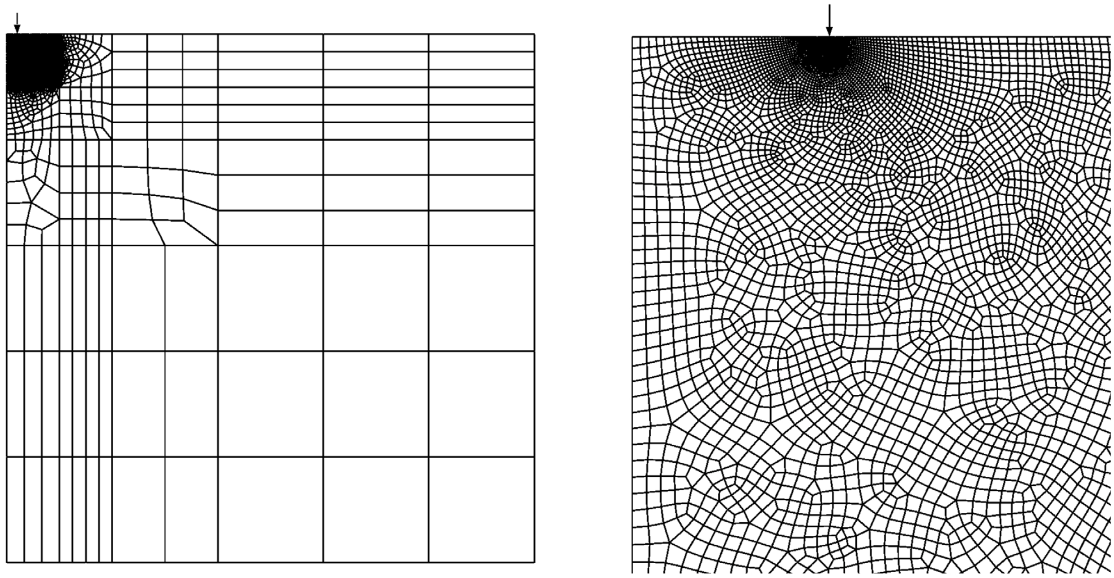

Fig. 4. Mesh 1 (coarse mesh). The arrow indicates the edge of the shallow footing.

represents the slope of the meridional section in triaxial compression conditions ($\theta = \pi/6$), whereas $\kappa(\bar{\varepsilon}_p)$ defines the intercept of the meridional section with the deviatoric stress axis in triaxial compression. Their evolution laws, which are responsible for the onset of softening in the considered problems, are specified separately for each constitutive model in the following subsections.

The numerical integration of the elastoplastic constitutive model is fully described by Panteghini and Lagioia (2014, 2018), and is employed here without any modification of the local constitutive integration, consistently with the black-box nature of the proposed formulation.

Four different meshes have been employed. The coarsest one is depicted in Fig. 4. Each subsequent mesh (Mesh 2, Mesh 3, Mesh 4) has been obtained by subdividing each element of the previous mesh into four elements. This deliberate choice avoids introducing preferred mesh orientations and allows for a systematic assessment of the mesh objectivity of the formulation.

The adopted finite elements are quadratic in the displacement field $\mathbf{u}$ and linear in the director field $\boldsymbol{\eta}$ (i.e., $n = 8$, $n_\eta = 4$). The internal force vector and the FE stiffness matrix are evaluated using four Gauss integration points. The main properties of the adopted meshes are summarized in Table 2.

All analyses have been performed using the commercial finite element code Abaqus (Dassault Systèmes, 2024). The proposed finite element formulation has been implemented through a user-defined element (UEL) subroutine.

4.1. Tresca cohesive soil

The elastic response of the soil under undrained conditions is modeled by assuming a shear modulus $G = 416.7\,\mathrm{MPa}$ and a bulk modulus $K_v = 55560\,\mathrm{MPa}$, corresponding to an elastic modulus $E = 1247\,\mathrm{MPa}$ and a Poisson ratio $\nu = 0.4963$. Since the undrained

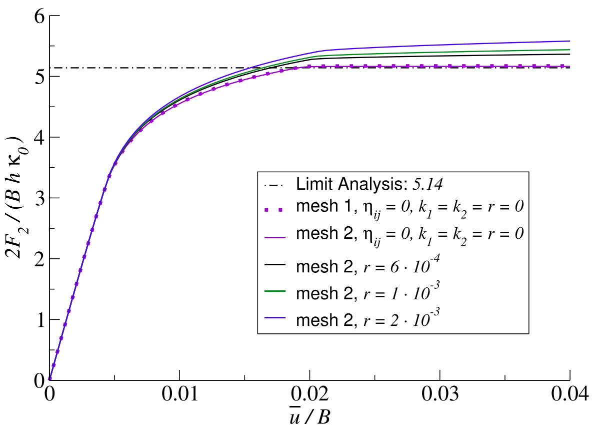

Fig. 5. Strip footing on a Tresca soil under perfect plasticity: normalized load–displacement curves. The Cauchy response (obtained by enforcing $\boldsymbol{\eta} = \mathbf{0}$ and $k_1 = k_2 = \ell = 0$) coincides with Prandtl's solution. Results for the deformable Cosserat continuum are shown for $r = \ell/B = 6 \cdot 10^{-4}$, 10^{-3}, and $2 \cdot 10^{-3}$, highlighting the recovery of the classical solution and the emergence of a mild size effect as r increases.

plastic response is pressure-independent, the parameter M is set equal to zero. Accordingly, the plastic rate tensor is traceless, i.e., $\mathbf{D}_p : \mathbf{I} = 0$. The accumulated plastic strain is defined as

$$\bar{\varepsilon}_p = \int \sqrt{\frac{2}{3}\mathbf{D}_p : \mathbf{D}_p}\,\mathrm{d}t. \tag{50}$$

Two constitutive responses are considered for the macro-continuum, namely perfect plasticity, $\kappa = \kappa_0$, and isotropic softening, defined as

$$\kappa = \kappa_\infty + (\kappa_0 - \kappa_\infty)\exp(-a_h \bar{\varepsilon}_p).$$

The softening parameters are chosen as $\kappa_0 = 980\,\mathrm{kPa}$, $\kappa_\infty = 9.8\,\mathrm{kPa}$ and $a_h = 10$.

All analyses are carried out under displacement control using the standard nonlinear static solver of Abaqus (Dassault Systèmes, 2024). The initial and maximum time increments are set equal to $10^{-4}\, t_0$ and $5 \cdot 10^{-3}\, t_0$, respectively, where t_0 is the (dummy) load time. The imposed normalized vertical displacement is $\bar{u}/B = 0.1$. No geostatic initial state and no lateral surcharge are considered, and a rough footing-soil interface is assumed. Unless otherwise specified, the micro-continuum parameters are set to $k_1 = k_2 = 0.1$.

Fig. 5 shows the normalized load–displacement curves obtained under perfect plasticity. In this case, only Mesh 1 and Mesh 2 are considered, since no mesh dependence is expected in the absence of softening. The classical Cauchy solution is recovered by enforcing $\boldsymbol{\eta} = \mathbf{0}$ at all nodes and setting $k_1 = k_2 = \ell = 0$, and coincides with Prandtl's solution (Prandtl, 1920). The deformable Cosserat results are obtained for $r = \ell/B = 6 \cdot 10^{-4}$, 10^{-3}, and $2 \cdot 10^{-3}$, showing that the proposed formulation correctly recovers the classical response in the limit case. Increasing r leads to a slightly stiffer response and a modest increase in the peak load, indicating the emergence of a size effect when the internal length becomes non-negligible with respect to the footing width.

The results obtained with exponential softening are reported in Fig. 6, in terms of load–displacement curves, total dissipated energy as functions of the applied displacement, and profiles of the accumulated plastic strain $\bar{\varepsilon}_p$ along the upper boundary of the domain. A clear convergence of the global response is observed upon mesh refinement, both for the load–displacement curves and for the total dissipated energy. The convergence of the entire dissipation history (and not only of its final value) further supports the consistency of the numerical results. The rate of convergence depends on the ratio $r = \ell/B$: for $r = 2 \cdot 10^{-3}$, Mesh 2 and Mesh 3 already provide essentially coincident results, and Mesh 4 is therefore not considered; for $r = 10^{-3}$, convergence is very good for all three meshes, while for $r = 6 \cdot 10^{-4}$, Mesh 2 is not yet converged and Mesh 3 and Mesh 4 are required to approach convergence. This behavior reflects the fact that smaller values of r lead to finer localization patterns, which require a higher spatial resolution. This is also confirmed by the profiles of $\bar{\varepsilon}_p$ reported in Fig. 6(c), plotted as functions of the normalized coordinate x_1/B with $x_1 = 0$ corresponding to the symmetry axis of the footing. The profiles provide a local representation of the regularized plastic zone and show that, for a fixed value of r, the spatial distribution of accumulated plastic strain becomes essentially mesh-independent upon refinement.

Before discussing the local fields, it was verified that, for the converged meshes considered in the contour plots reported below, the dominant shear bands are resolved by a sufficiently large number of elements across their thickness, without spurious jumps appearing when contour averaging is disabled. For this reason, the contour plots are reported without superimposing the full underlying mesh, since for the finest discretizations this would make the figures largely unreadable without improving the evaluation of the localization pattern.

Fig. 7 shows the normalized displacement magnitude, $|\mathbf{u}|/B$, for the Tresca model at the last loading increment. Results are obtained with Mesh 3 for $r = 6 \times 10^{-4}$ and $r = 2 \cdot 10^{-3}$. The contours are plotted on the deformed configuration with a displacement scale factor equal to one and show a smooth displacement field without spurious discontinuities or interpenetration.

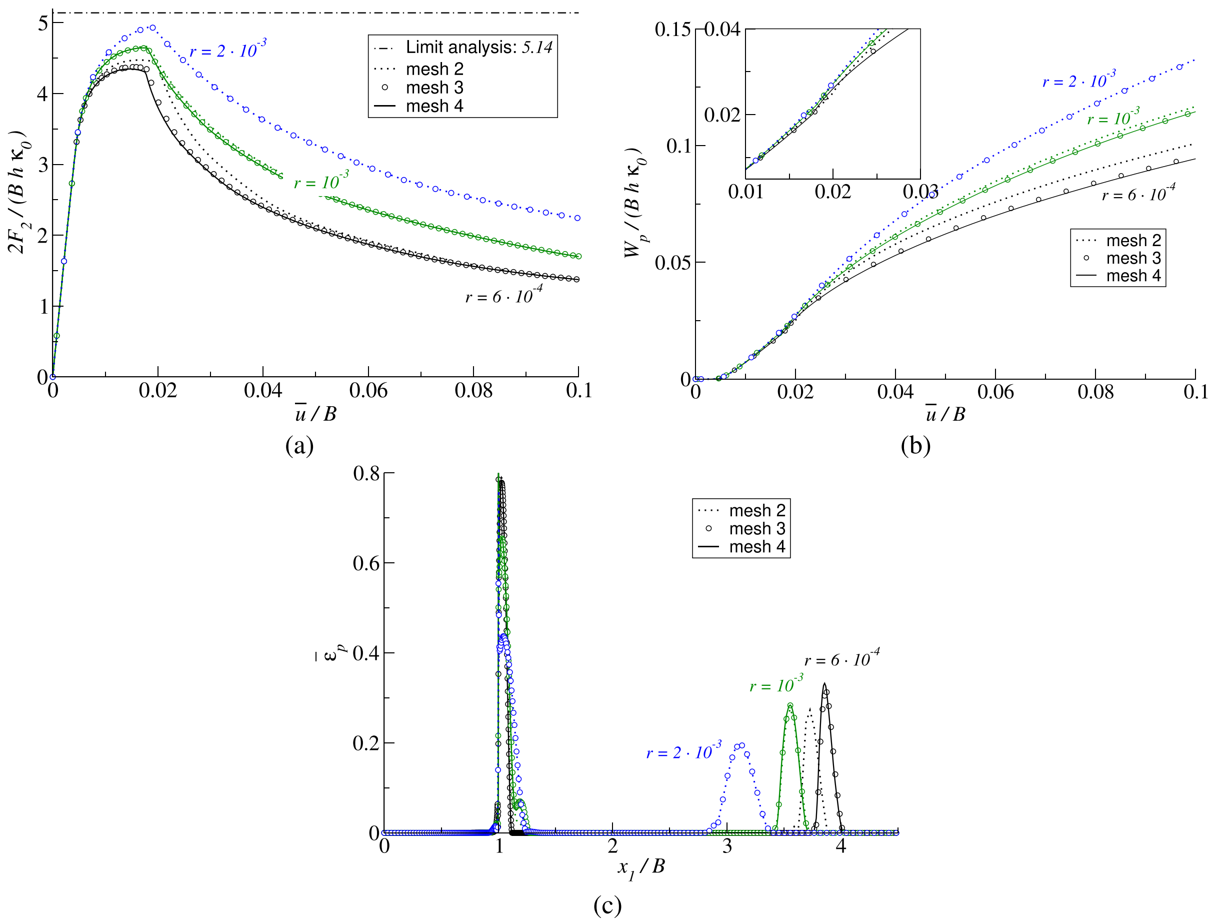

Fig. 6. Strip footing on a Tresca soil with exponential isotropic softening: (a) normalized load–displacement curves, (b) total dissipated energy as a function of the applied displacement, and (c) profiles of the accumulated plastic strain $\bar{\varepsilon}_p$ along the upper boundary of the domain, plotted against the normalized horizontal coordinate x_1/B, at the final step. The coordinate $x_1 = 0$ corresponds to the symmetry axis of the footing. Results are reported for different values of $r = \ell/B$ and for multiple meshes, showing convergence of both the global response and the dissipation history upon mesh refinement, together with the regularized spatial distribution of accumulated plastic strain along the upper boundary.

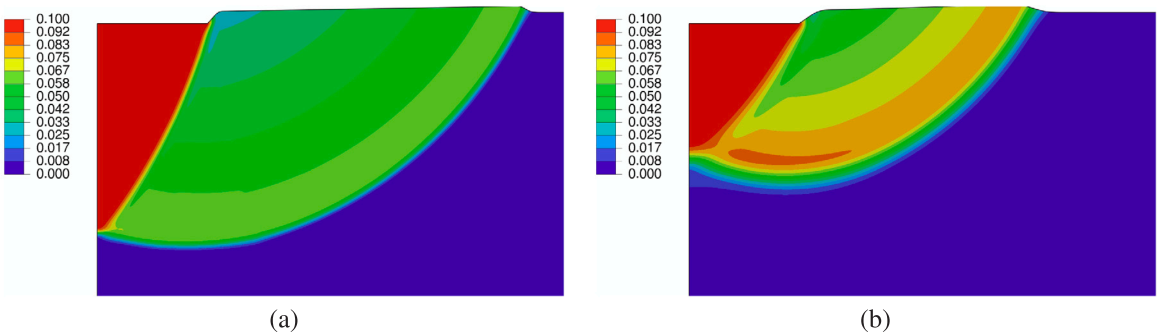

Fig. 7. Normalized displacement magnitude $|\mathbf{u}|/B$ for the strip footing on Tresca soil with exponential isotropic softening at the last loading increment (Mesh 3). Results are plotted on the deformed configuration with a displacement scale factor equal to one: (a) $r = 6 \cdot 10^{-4}$ and (b) $r = 2 \cdot 10^{-3}$.

The localization patterns are analyzed by considering the spatial distribution of κ, which is a monotonically decreasing quantity and therefore allows a direct identification of the shear bands as regions of minimum κ. For $r = 2 \cdot 10^{-3}$ (Fig. 8), the pattern closely resembles the classical Prandtl mechanism, with two dominant shear bands and a slightly diffuse region between them.

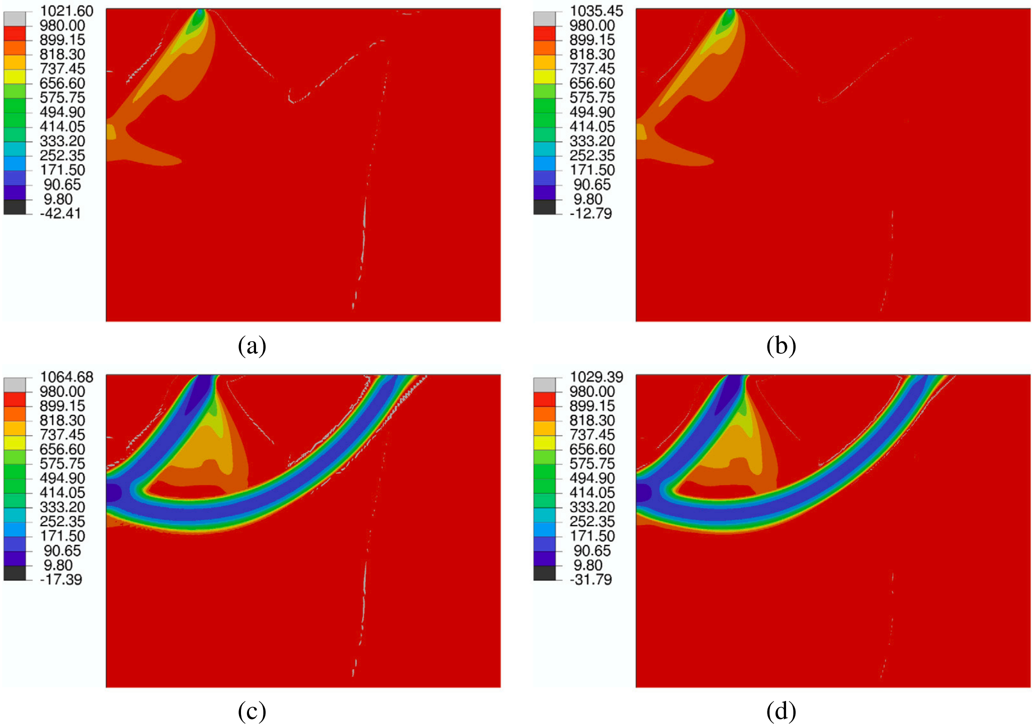

Fig. 8. Spatial distribution of κ (in kPa) for the strip footing on Tresca soil with exponential softening, $r = 2 \cdot 10^{-3}$. (a)–(b) Mesh 2 and Mesh 3 at peak load; (c)–(d) Mesh 2 and Mesh 3 at the end of the analysis ($\bar{u}/B = 0.1$). The localization pattern, consisting of two dominant shear bands with a slightly diffuse intermediate zone, is essentially coincident across meshes, indicating mesh objectivity.

Table 3
Numerical performance for the strip footing on Tresca soil with exponential softening, in terms of number of load increments and total iterations. Comparable values across meshes confirm the robustness of the formulation, with slightly higher computational effort for smaller values of $r = \ell/B$.

r	Mesh 2		Mesh 3		Mesh 4	
	Loading steps	Total iterations	Loading steps	Total iterations	Loading steps	Total iterations
$6 \cdot 10^{-4}$	241	930	250	1124	260	1314
10^{-3}	222	725	229	877	238	1057
$2 \cdot 10^{-3}$	211	566	216	650	/	/

The results obtained with Mesh 2 and Mesh 3 are essentially coincident, indicating mesh objectivity. For $r = 10^{-3}$ (Fig. 9), the localization pattern becomes significantly richer, with the development of a network of secondary shear bands. Both primary and secondary bands are almost perfectly coincident across meshes, showing that the formulation captures even fine-scale features in a mesh-independent manner. It is important to emphasize that ℓ is a *material* parameter, not a *smoothing* parameter. The value of ℓ for a given material depends on microstructure, and should therefore be regarded as a constitutive length scale controlling the regularized localization pattern, rather than as a numerical parameter adjusted to obtain mesh convergence.

For the smallest value $r = 6 \cdot 10^{-4}$ (Fig. 10), the pattern becomes even more intricate, with a dense network of secondary bands. The main shear bands are well captured and essentially coincident, whereas some differences persist in the finer secondary structures, indicating that an even finer mesh would be required to fully resolve all details. It is worth noting that the convergence of local fields is more demanding than that of global quantities such as load–displacement curves or dissipated energy, which converge faster with mesh refinement.

These results highlight that the internal length scale does not merely enforce mesh objectivity, but also governs the emergence of different localization mechanisms, leading to qualitatively different failure patterns as the ratio $r = \ell/B$ is varied.

The numerical performance of the simulations is summarized in Table 3. The number of load increments and total iterations remain comparable across different meshes, confirming the robustness of the formulation. The most demanding case corresponds to $r = 6 \cdot 10^{-4}$, where the average time increment remains close to the maximum allowable value (76.9% of the maximum allowable time increment) and the average number of iterations per increment is approximately 5.05, indicating a stable nonlinear solution process even in the presence of strong softening.

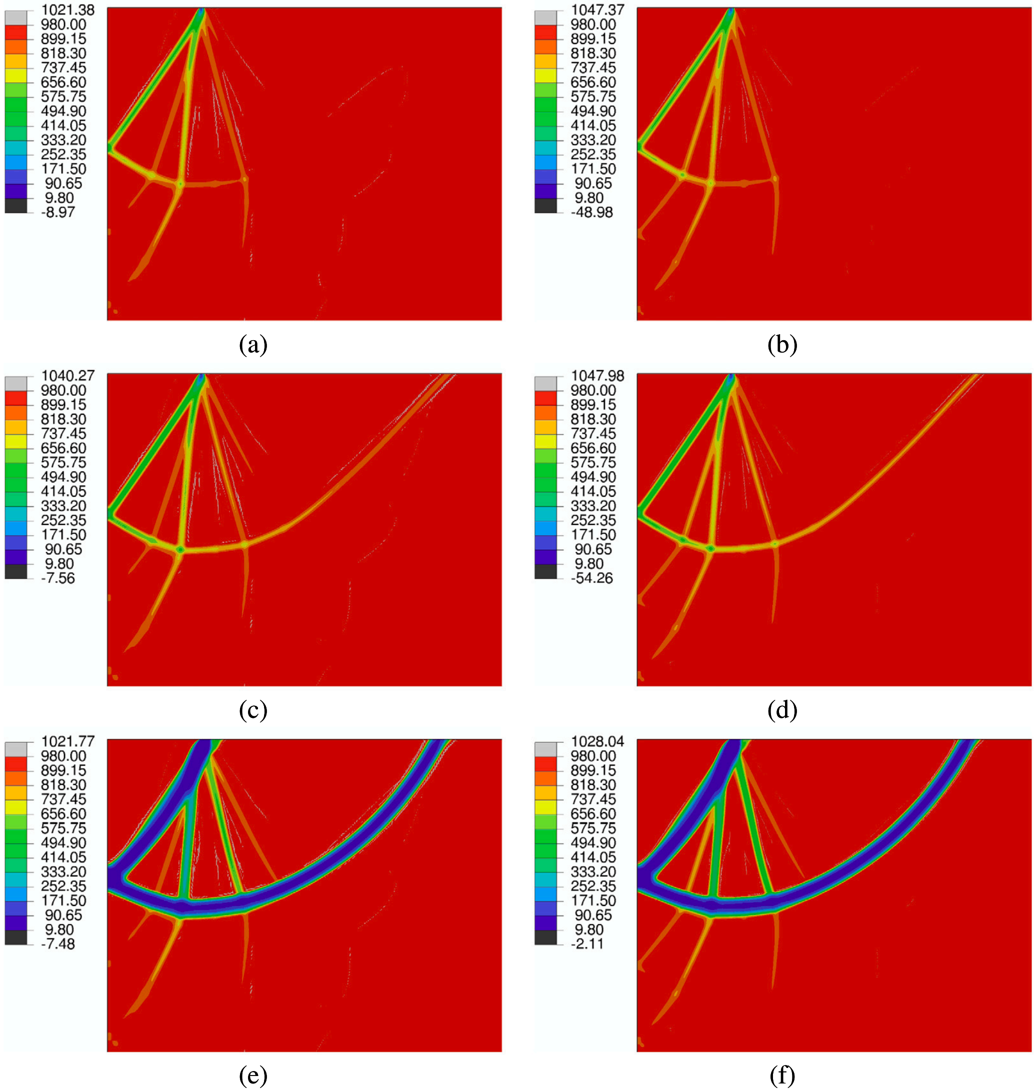

Fig. 9. Spatial distribution of κ (in kPa) for the strip footing on Tresca soil with exponential softening, $r = 10^{-3}$. (a)–(b) Mesh 3 and Mesh 4 at peak load; (c)–(d) at $\bar{u}/B = 0.02$; (e)–(f) at the end of the analysis ($\bar{u}/B = 0.1$). In addition to the main shear bands, a network of secondary bands develops. Both primary and secondary structures are nearly coincident across meshes, demonstrating mesh-independent prediction of complex localization patterns.

Finally, Fig. 11 shows the influence of the micro-elastic parameters k_1 and k_2 for $r = 10^{-3}$ and $r = 2 \cdot 10^{-3}$. Notice that increasing $k_1 = k_2$ tends to increase the peak load but has little effect on the final load. The results indicate that the global response is only moderately affected by these parameters and tends to saturate for larger values. No significant changes in the localization patterns are observed, suggesting that the internal length plays a dominant role in governing the structural response.

4.2. Matsuoka–Nakai soil subject to self-weight

These analyses are conducted using the Matsuoka–Nakai criterion (Matsuoka & Nakai, 1974; Panteghini & Lagioia, 2014), a constitutive model commonly adopted to describe drained soil behavior. The elastic response is assumed to be linear, with shear modulus $G = 41.67\,\mathrm{MPa}$ and bulk modulus $K_v = 55.56\,\mathrm{MPa}$.

The soil is dry, with unit weight $\gamma_0 = 18\,\mathrm{kN/m^3}$. Two sets of material parameters are considered, namely: (i) perfect plasticity, with no cohesion ($\kappa = 0$) and constant angle of shearing resistance $\phi = \phi_0 = 30°$, and (ii) a softening response, associated with a constant cohesion (modeled by assuming $\kappa = 8\,\mathrm{kPa}$) and a decreasing angle of shearing resistance. For the latter case, ϕ is assumed to evolve according to a piecewise linear law as a function of the accumulated plastic strain $\bar{\varepsilon}_p$. In particular, ϕ decreases linearly

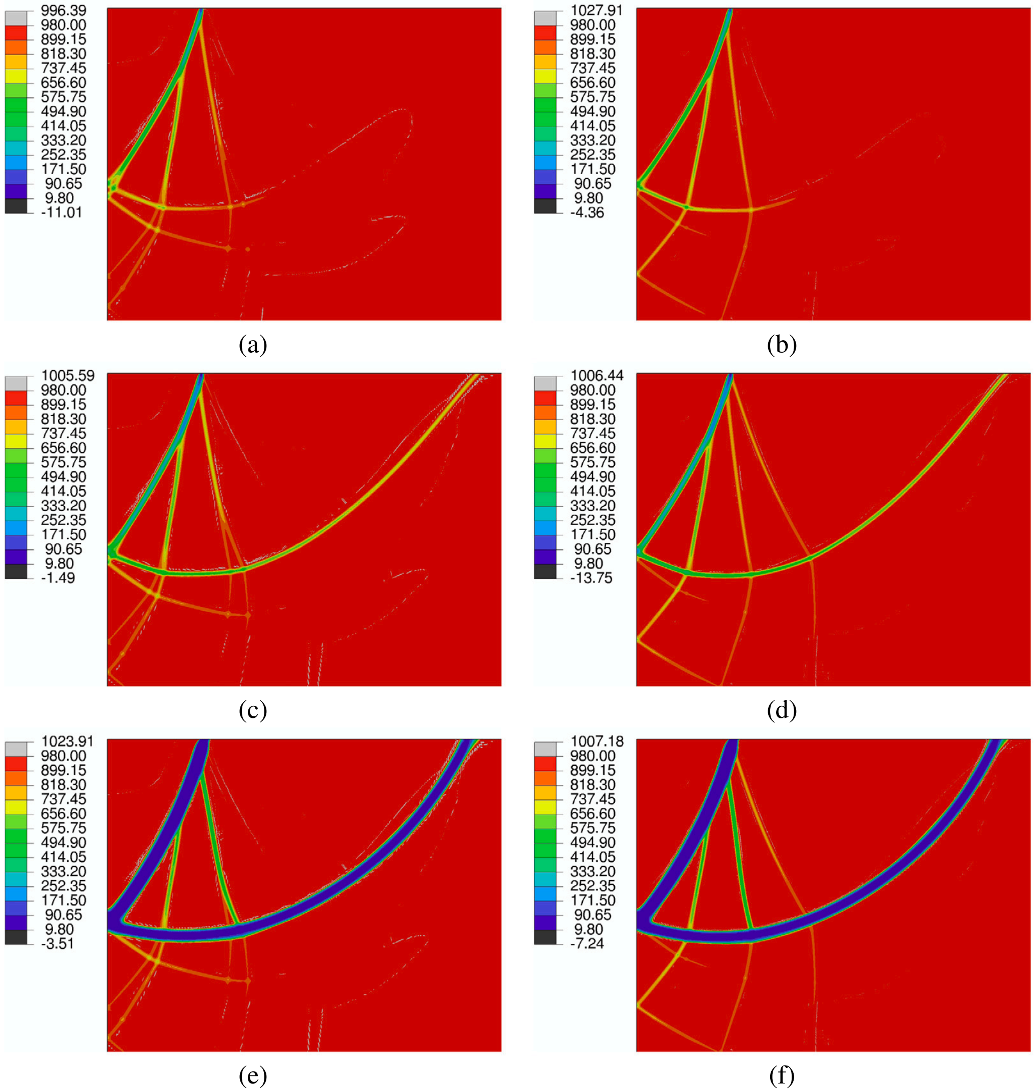

Fig. 10. Spatial distribution of κ (in kPa) for the strip footing on Tresca soil with exponential softening, $r = 6 \cdot 10^{-4}$. (a)–(b) Mesh 3 and Mesh 4 at peak load; (c)–(d) at $\bar{u}/B = 0.02$; (e)–(f) at the end of the analysis ($\bar{u}/B = 0.1$). The main shear bands are well captured and essentially coincident, whereas minor differences remain in the finer secondary structures, indicating that a finer discretization is required to fully resolve all localization features.

from $\phi_0 = 20°$ to $\phi_u = 10°$ over the interval $0 \le \bar{\varepsilon}_p \le \bar{\varepsilon}_p^u = 0.1$, and remains constant thereafter:

$$\phi(\bar{\varepsilon}_p) = \begin{cases} \phi_0 - \dfrac{\phi_0 - \phi_u}{\bar{\varepsilon}_p^u}\, \bar{\varepsilon}_p, & 0 \le \bar{\varepsilon}_p \le \bar{\varepsilon}_p^u, \\ \phi_u, & \bar{\varepsilon}_p > \bar{\varepsilon}_p^u. \end{cases} \tag{51}$$

The corresponding evolution of the material parameter M is obtained from the current value of ϕ through Eq. (49).

Since volumetric plastic deformations may occur, a different definition of the accumulated plastic strain is adopted with respect to the Tresca case, i.e.,

$$\bar{\varepsilon}_p = \int \dot{\lambda}\, \mathrm{d}t, \tag{52}$$

where $\dot{\lambda}$ is the plastic multiplier, as defined by Panteghini and Lagioia (2018).

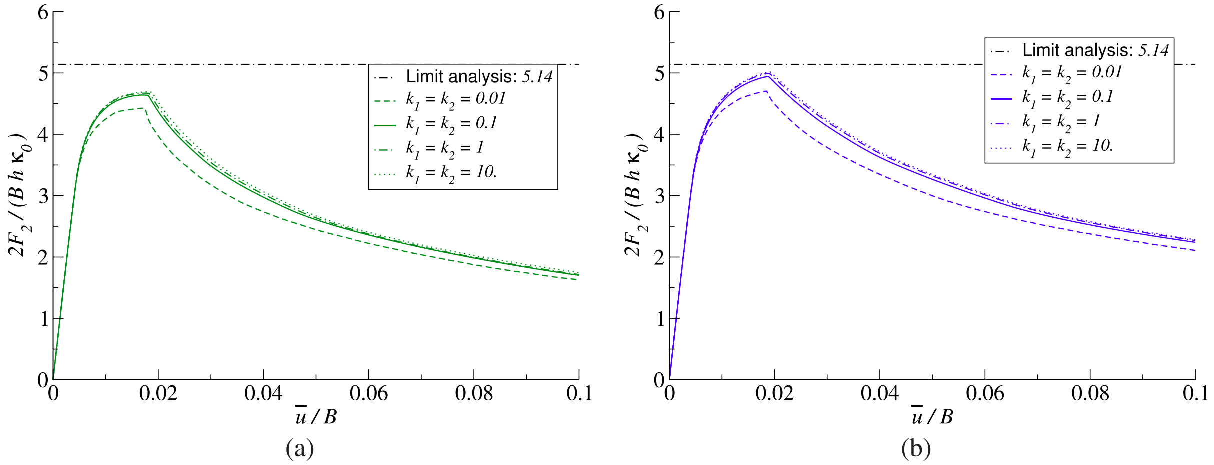

Fig. 11. Influence of the micro-elastic parameters k_1 and k_2 on the load–displacement response for the strip footing foundation on Tresca soil with exponential softening. Results are shown for Mesh 3, (a) $r = 10^{-3}$ and (b) $r = 2 \cdot 10^{-3}$. The response is only moderately affected and tends to saturate for increasing values of k_1 and k_2, while no significant changes in the localization patterns are observed.

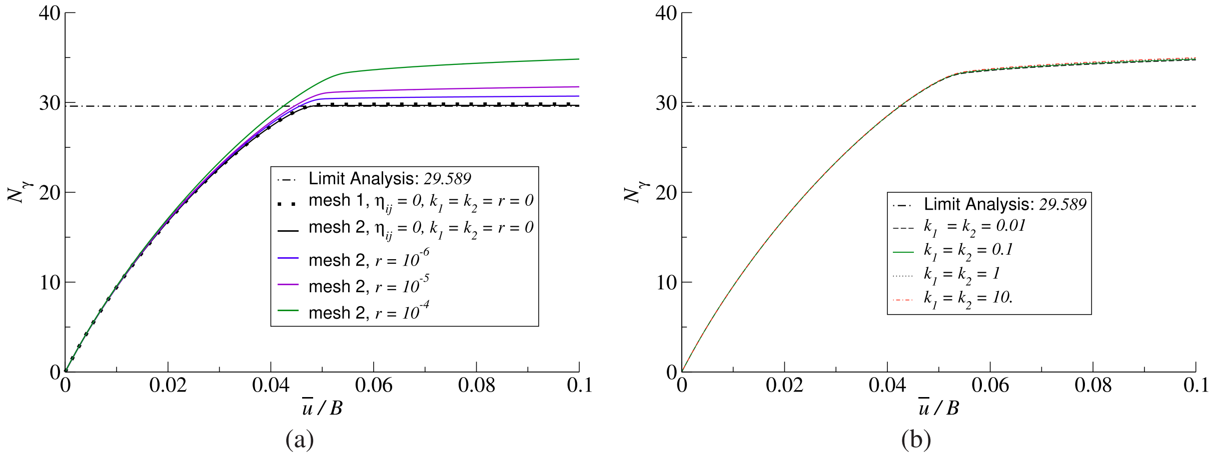

Fig. 12. Strip footing on Matsuoka–Nakai soil under perfect plasticity (N_γ problem). (a) Normalized load–displacement curves for different values of $r = \ell / B$, showing convergence to the classical Cauchy solution. (b) Influence of the micro-elastic parameters k_1 and k_2 for $r = 10^{-4}$, Mesh 2: the curves are practically coincident, indicating a negligible effect of these parameters on the global response.

A geostatic initial stress state is introduced to account for the soil self-weight. The vertical stress T_{22} is in equilibrium with the body forces due to the soil weight, while the initial horizontal and out-of-plane stresses are assumed as:

$$T_{11} = T_{33} = T_{22} \left(1 - \sin \phi_0\right). \tag{53}$$

The load is applied by prescribing the vertical displacement of the footing nodes. No lateral surcharge is applied, and a rough footing–soil interface is assumed. Unless otherwise specified, the micro-continuum parameters are set equal to $k_1 = k_2 = 0.1$.

The perfect plastic case corresponds to the classical N_γ problem. This benchmark is known to be particularly demanding from a numerical standpoint: in the absence of cohesion and lateral confinement, the yield condition is satisfied at the ground surface, while the elastic domain develops with depth due to the geostatic stress field. As a result, very steep stress gradients arise in the vicinity of the footing–soil interface. The analyses of the N_γ problem are performed using the standard nonlinear static solver of Abaqus (Dassault Systèmes, 2024). The initial and maximum time increments are set equal to $10^{-4}\, t_0$ and $5 \cdot 10^{-3}\, t_0$, respectively, where t_0 is a dummy load time. The imposed normalized vertical displacement is $\bar{u}/B = 0.1$.

Fig. 12a shows the normalized load–displacement curves obtained under perfect plasticity. The dimensionless load is defined as

$$N_\gamma = \frac{F_2}{B\, \gamma_0}, \tag{54}$$

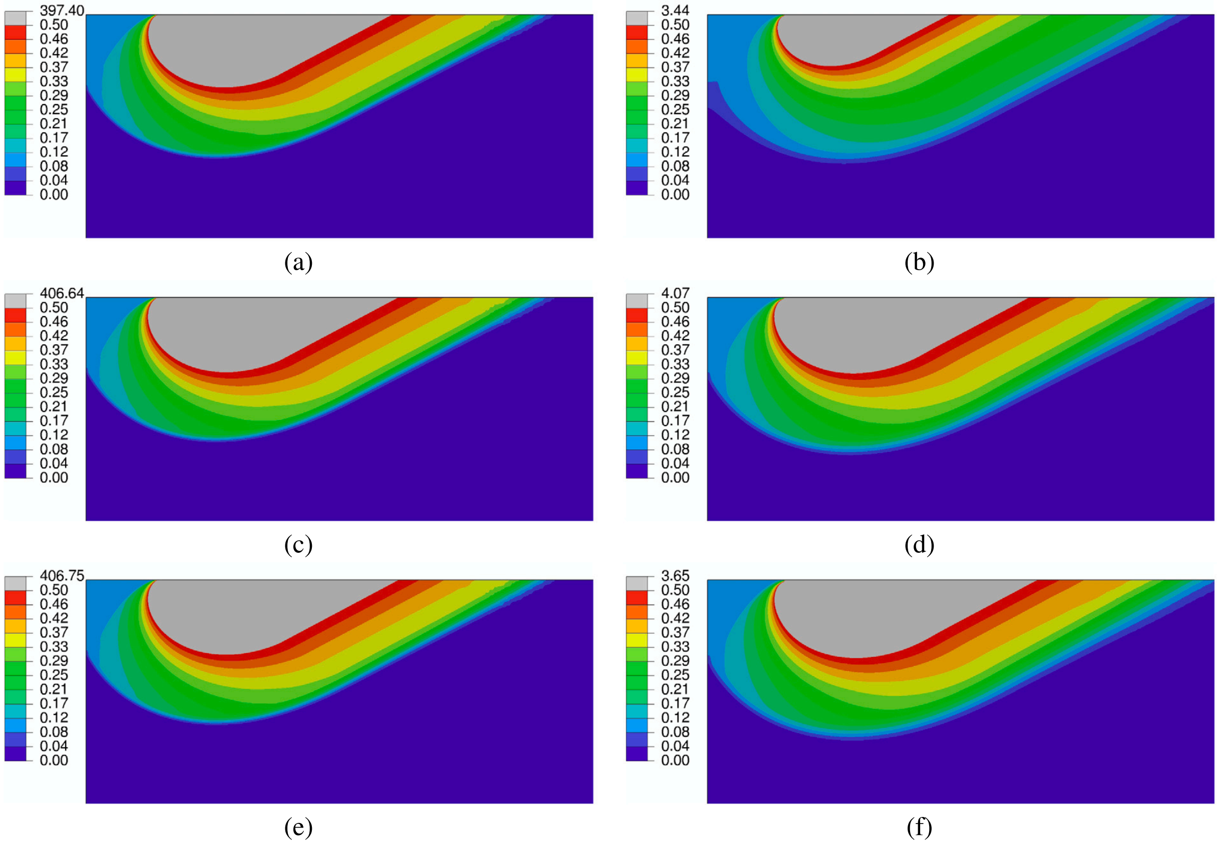

Fig. 13. Comparison between $|\dot{\mathbf{u}}|$ (in $\mathrm{m/s}$) obtained with Mesh 2 for the Cauchy continuum (a-c-e) and for $r = 10^{-4}$ (b-d-f) at different loading levels for the N_γ problem. (a) Cauchy, $\bar{u}/B = 0.05$, (b) $r = 10^{-4}$, $\bar{u}/B = 0.05$. (c) Cauchy, $\bar{u}/B = 0.07$, (d) $r = 10^{-4}$, $\bar{u}/B = 0.07$. (e) Cauchy, $\bar{u}/B = 0.1$ (end of the analysis), (f) $r = 10^{-4}$, $\bar{u}/B = 0.1$ (end of the analysis).

where F_2 is the resultant vertical reaction per unit depth at the footing.

Only Mesh 1 and Mesh 2 are considered, since no mesh dependence is expected in the absence of softening. The classical Cauchy solution is recovered by enforcing $\boldsymbol{\eta} = \mathbf{0}$ at all nodes and setting $k_1 = k_2 = \ell = 0$. The reference solution is obtained from limit analysis using the method of characteristics, computed with the ABC code developed by Martin (2003, 2004) and extended to general yield criteria following Lagioia and Panteghini (2017).

The deformable Cosserat results are reported for $r = \ell/B = 10^{-6}$, 10^{-5}, and 10^{-4}. The results show that the proposed formulation recovers the classical response in the limit $r \to 0$. Increasing r leads to a slightly stiffer response and to a modest increase in the peak load, indicating the emergence of a size effect when the internal length becomes non-negligible compared to the footing width.

Fig. 12b shows the influence of the micro-elastic parameters k_1 and k_2 for $r = 10^{-4}$. The curves are essentially coincident, indicating that the global response is weakly affected by these parameters under perfect plasticity.

Fig. 13 shows the spatial distribution of the velocity magnitude at different loading stages, for both the Cauchy continuum and the Cosserat model with $r = 10^{-4}$. Since the response is rate-independent the magnitude of the velocity is a relative quantity. In the Cosserat case, the magnitude of the velocity is approximately two orders of magnitude smaller than in the classical solution, indicating a more distributed deformation process and a reduced tendency towards instantaneous localization.

The softening response is characterized by a pronounced loss of strength associated with the reduction of the angle of shearing resistance (see Fig. 14). As a result, the global load–displacement response exhibits a non-monotonic behavior with a distinct post-peak regime, including an *unstable* region. For this reason, the analyses cannot be performed using a standard displacement-controlled procedure and are instead carried out using an arc-length method (de Souza Neto et al., 2008). In particular, the Riks algorithm available in Abaqus (Dassault Systèmes, 2024) is adopted. The initial arc-length increment is set equal to $1 \cdot 10^{-4}$, with a maximum increment equal to $5 \cdot 10^{-3}$. The analyses have been stopped at the first increment in which $\bar{u}/B \geq 0.05$.

The convergence properties of the proposed formulation are first assessed by considering the smallest value of the normalized internal length adopted in this study, namely $r = \ell/B = 4.5 \cdot 10^{-4}$. This choice corresponds to the most demanding case in terms of localization, as smaller values of r lead to increasingly complicated deformation patterns and sharper strain gradients.

It should be noted that the values of r adopted in the present softening analyses are larger than those used for the N_γ problem under perfect plasticity. This is intentional: in the absence of softening, very small values of r can be employed to recover the

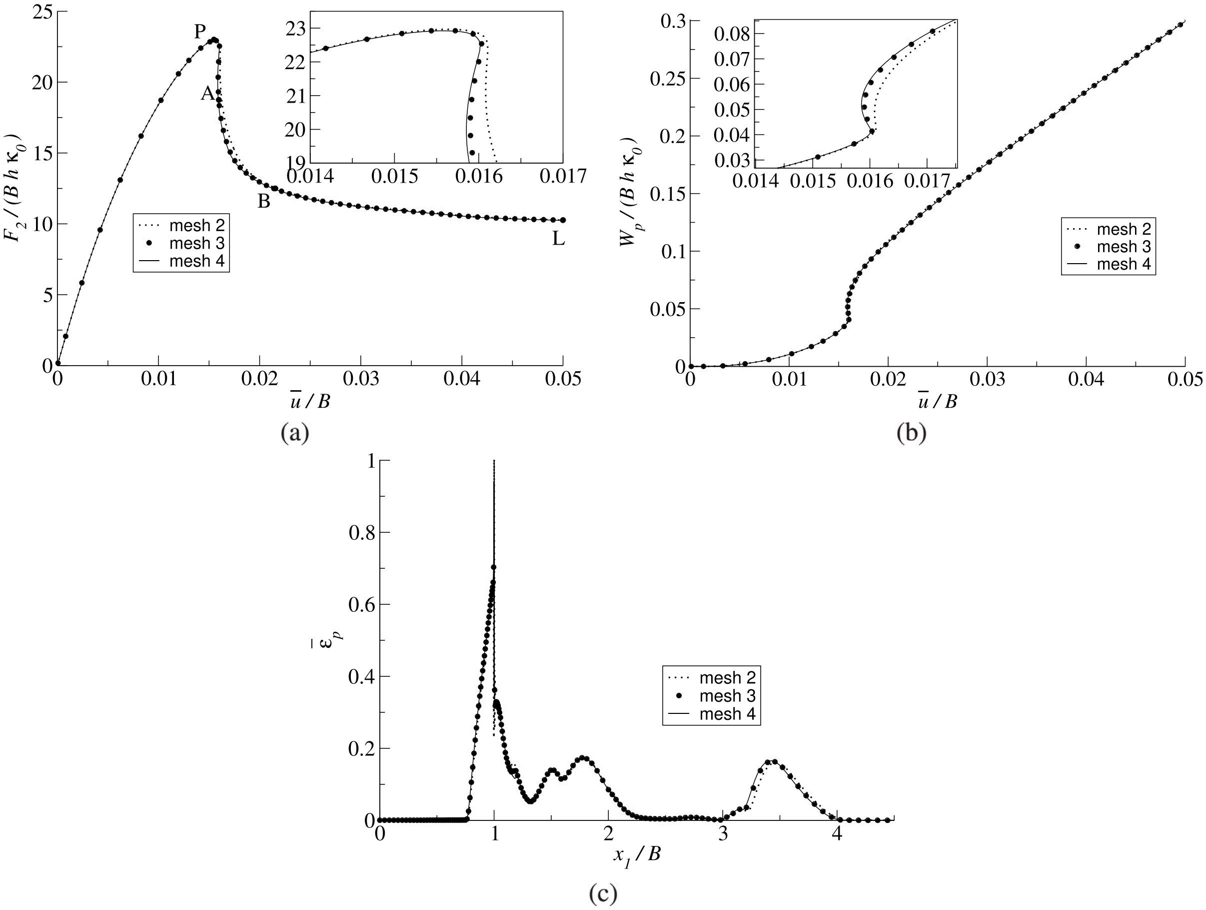

Fig. 14. Convergence of the solution for the strip footing on Matsuoka–Nakai soil with softening, obtained using the Riks procedure for $r = 4.5 \cdot 10^{-4}$: (a) load–displacement curves, (b) dissipated energy as a function of the normalized footing displacement, and (c) profiles of the accumulated plastic strain $\bar{\varepsilon}_p$ along the upper boundary of the domain, plotted against the normalized horizontal coordinate x_1/B, at the final step. The coordinate $x_1 = 0$ corresponds to the symmetry axis of the footing, and the prescribed footing displacement is applied over the footing width only. The global responses in (a) and (b) exhibit a non-monotonic evolution with a pronounced post-peak regime associated with unstable behavior, while showing clear convergence upon mesh refinement; the profiles in (c) illustrate the corresponding spatial distribution of accumulated plastic strain along the upper boundary.

classical Cauchy solution, whereas in the presence of strong strain softening, the choice of r must ensure an adequate resolution of the localization mechanisms within a feasible mesh discretization.

Fig. 14 shows the convergence of the solution in terms of load–displacement curves (a), dissipated energy as a function of the strip footing displacement (b), and profiles of the accumulated plastic strain $\bar{\varepsilon}_p$ along the upper boundary of the domain (c). The two global responses in Fig. 14(a,b) exhibit a non-monotonic response with a pronounced post-peak regime due to the unstable behavior. Despite the presence of an unstable behavior, the load–displacement curves obtained with Mesh 3 and Mesh 4 are essentially coincident, indicating convergence of the global response. The same conclusion can be drawn from the dissipated energy, reported as a function of the strip footing displacement in Fig. 14(b). The entire dissipation history converges with mesh refinement, further confirming the consistency of the formulation. The profiles of $\bar{\varepsilon}_p$ reported in Fig. 14(c), plotted as functions of the normalized coordinate x_1/B with $x_1 = 0$ corresponding to the symmetry axis of the footing, provide a local measure of the regularized plastic zone. The close agreement between Mesh 3 and Mesh 4 shows that the spatial distribution of accumulated plastic strain is also essentially mesh-independent upon refinement.

The spatial distribution of ϕ, reported in Fig. 15, shows that the localization patterns are also fully converged between Mesh 3 and Mesh 4. In particular, both the primary and secondary shear bands are coincident during all their evolution, indicating that, in the present benchmark, the proposed formulation is able to capture complex localization mechanisms in a mesh-independent manner even in the presence of strong softening and unstable structural response.

It is worth emphasizing that, compared to the Tresca case discussed in the previous section, the convergence behavior is improved, despite the more severe nonlinear response. This further supports the robustness of the proposed approach for the class of problems investigated here.

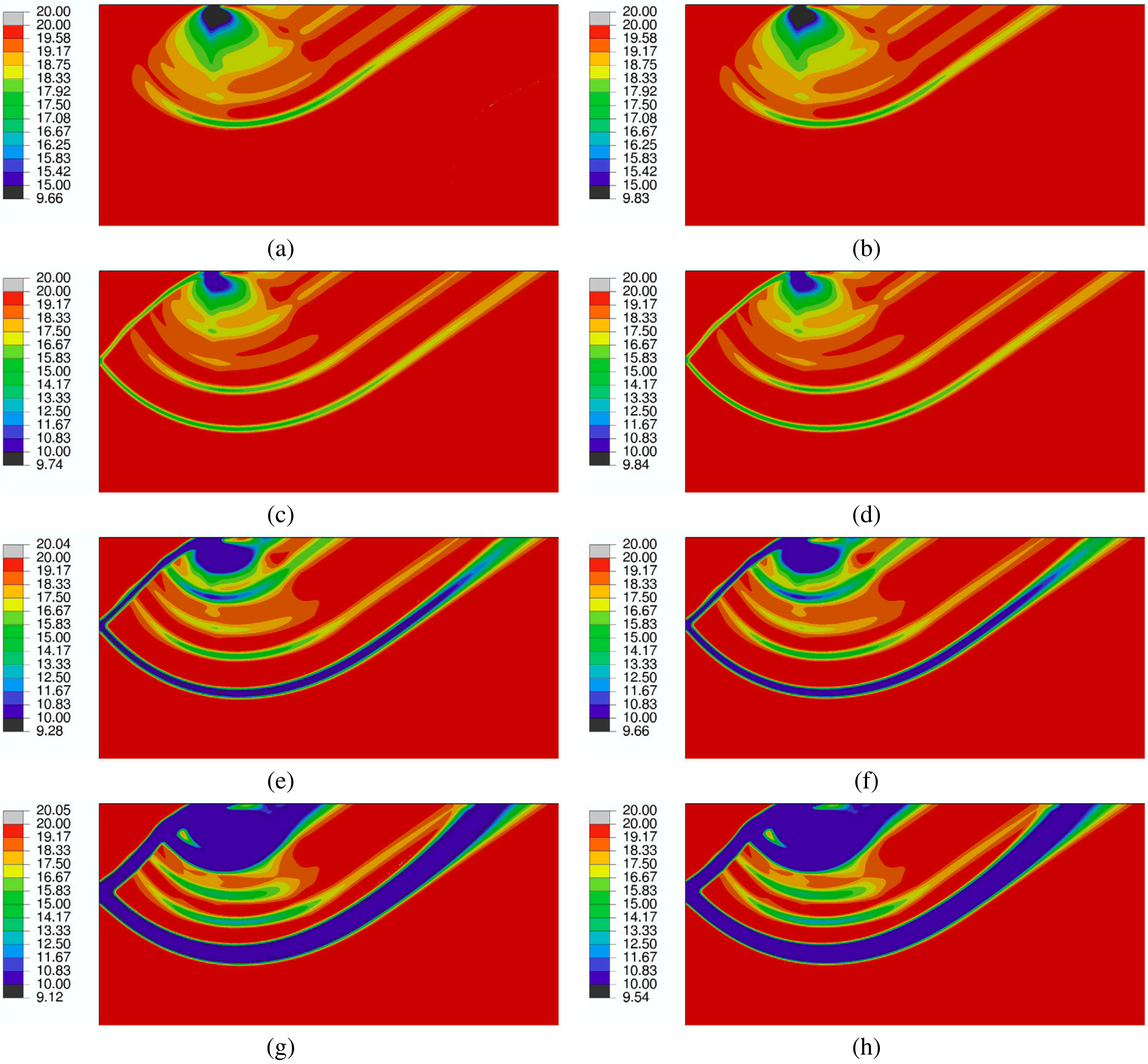

Fig. 15. Convergence of the ϕ profiles (in degrees) for $r = 4.5 \cdot 10^{-4}$. (a) Mesh 3, stress peak (point P of Fig. 14a), (b) Mesh 4, stress peak (point P of Fig. 14a). (c) Mesh 3, point A of Fig. 14a, (d) Mesh 4, point A of Fig. 14a. (e) Mesh 3, point B of Fig. 14a, (f) Mesh 4, point B of Fig. 14a. (g) Mesh 3, point L of Fig. 14a, (h) Mesh 4, point L of Fig. 14a.

The computational cost of the analyses is summarized in Table 4. The average number of iterations per increment is 2.23 for Mesh 2, 2.35 for Mesh 3 and 2.36 for Mesh 4. The average arc-length increment is $4.88 \cdot 10^{-3}$ for Mesh 2 and $4.84 \cdot 10^{-3}$ for Mesh 3 and Mesh 4. It is worth noting that the average number of iterations per increment remains low, and that the arc-length increment is very close to the maximum allowable value, set equal to $5 \cdot 10^{-3}$. These results indicate a very stable nonlinear solution process, even in the presence of a pronounced softening response related to an unstable behavior. Moreover, the computational cost is essentially independent of the mesh refinement, further confirming the robustness of the proposed formulation.

The influence of the internal length is further investigated by considering different values of the normalized parameter $r = \ell / B$, namely $r = 4.5 \cdot 10^{-4}$, $6 \cdot 10^{-4}$, $8 \cdot 10^{-4}$, and 10^{-3}. Fig. 16 shows the corresponding load–displacement curves. A strong dependence of the global response on the internal length is observed. For the smallest values, $r = 4.5 \cdot 10^{-4}$ and $r = 6 \cdot 10^{-4}$, the response exhibits a pronounced softening behavior with an unstable post-peak regime. In contrast, for larger values of r, the response becomes progressively smoother, with reduced softening and more stable post-peak evolution.

Fig. 17 shows the normalized displacement magnitude, $|\mathbf{u}|/B$, for the Matsuoka–Nakai model at the last computed equilibrium state of the Riks analysis. Results are obtained with Mesh 3 for $r = 4.5 \cdot 10^{-4}$ and $r = 10^{-3}$. The contours are plotted on the deformed

Table 4
Numerical performance for the strip footing on Matsuoka–Nakai soil with linear softening of the angle of shearing resistance, in terms of number of load increments and total nonlinear iterations, for $r = 4.5 \cdot 10^{-4}$ using the Riks procedure. The results are very similar across meshes, indicating mesh-independent computational cost and a robust solution procedure despite the presence of an unstable behavior.

Mesh	Loading steps	Total iterations	Total arc length
2	358	799	1.75
3	361	850	1.75
4	361	855	1.75

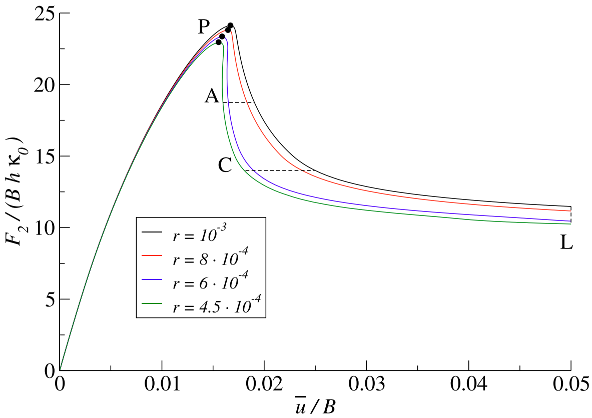

Fig. 16. Influence of the internal length $r = \ell / B$ on the load–displacement response for the Matsuoka–Nakai model with softening (Mesh 3). Smaller values of r lead to a more pronounced softening and to an unstable post-peak response, whereas larger values produce a smoother and more stable behavior.

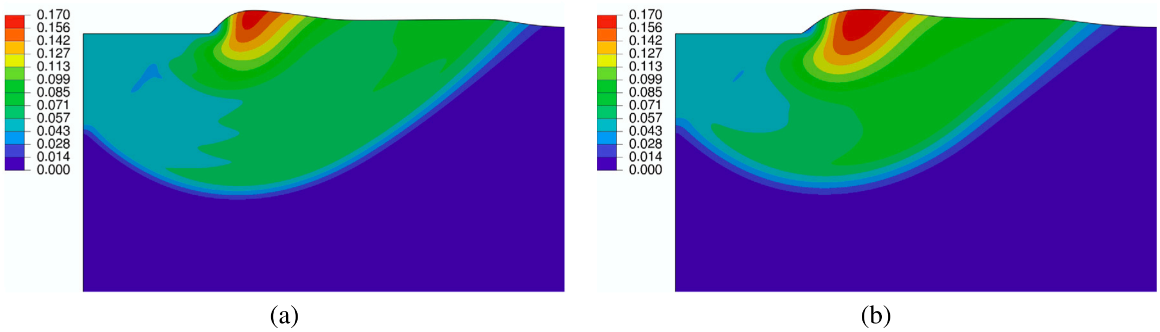

Fig. 17. Normalized displacement magnitude $|\mathbf{u}|/B$ for the strip footing on Matsuoka–Nakai model with softening at the last computed equilibrium state of the Riks analysis (Mesh 3). Results are plotted on the deformed configuration with a displacement scale factor equal to one: (a) $r = 4.5 \cdot 10^{-4}$ and (b) $r = 10^{-3}$.

configuration with a displacement scale factor equal to one and show a smooth displacement field without spurious discontinuities or interpenetration.

The localization patterns are shown in Figs. 18–21 in terms of the spatial distribution of the angle of shearing resistance ϕ, at different loading stages (point P peak load, point A, point C and final step L). A qualitative change in the deformation mechanisms is observed as the internal length varies. For the smallest values of r, the localization pattern is characterized by the development of multiple shear bands, which appear approximately parallel to those associated with the classical limit analysis solution. These bands form a complex network of interacting localization zones, indicating a highly localized deformation process. For larger values of r, the deformation pattern becomes significantly simpler. The response is dominated by two main shear bands, consistent with

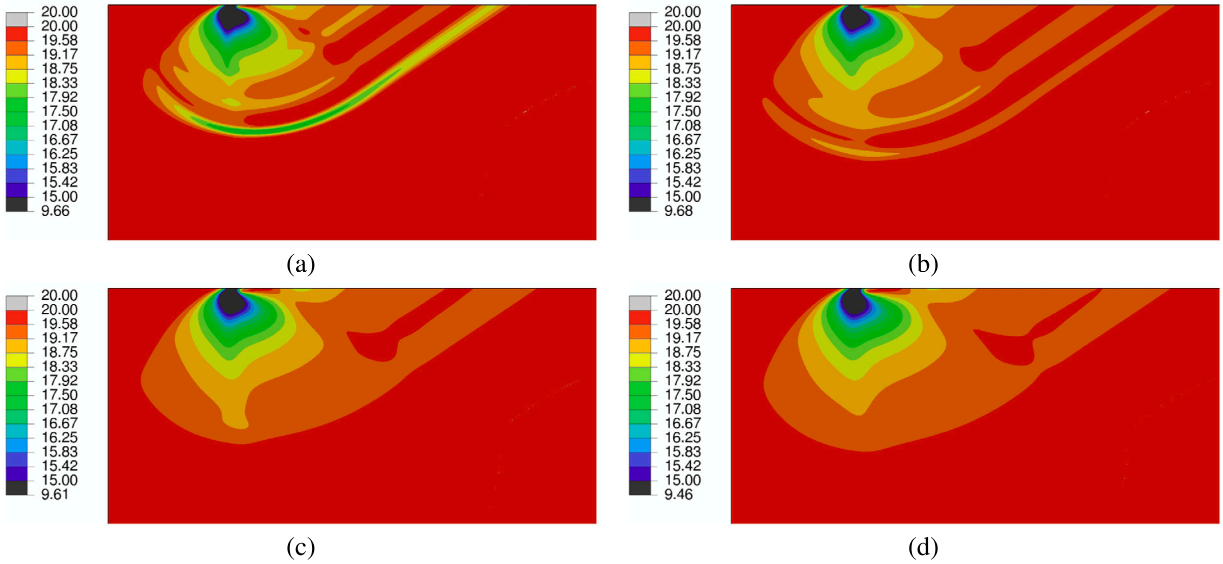

Fig. 18. Spatial distribution of the angle of shearing resistance ϕ (in degrees) for different values of $r = \ell/B$, at peak load (point P in Fig. 16), for Mesh 3. (a) $r = 4.5 \cdot 10^{-4}$, (b) $r = 6 \cdot 10^{-4}$, (c) $r = 8 \cdot 10^{-4}$, (d) $r = 10^{-3}$. Smaller values of r lead to the development of multiple shear bands, approximately parallel to the limit analysis solution, while larger values promote simpler mechanisms with two dominant shear bands and a more diffuse intermediate region.

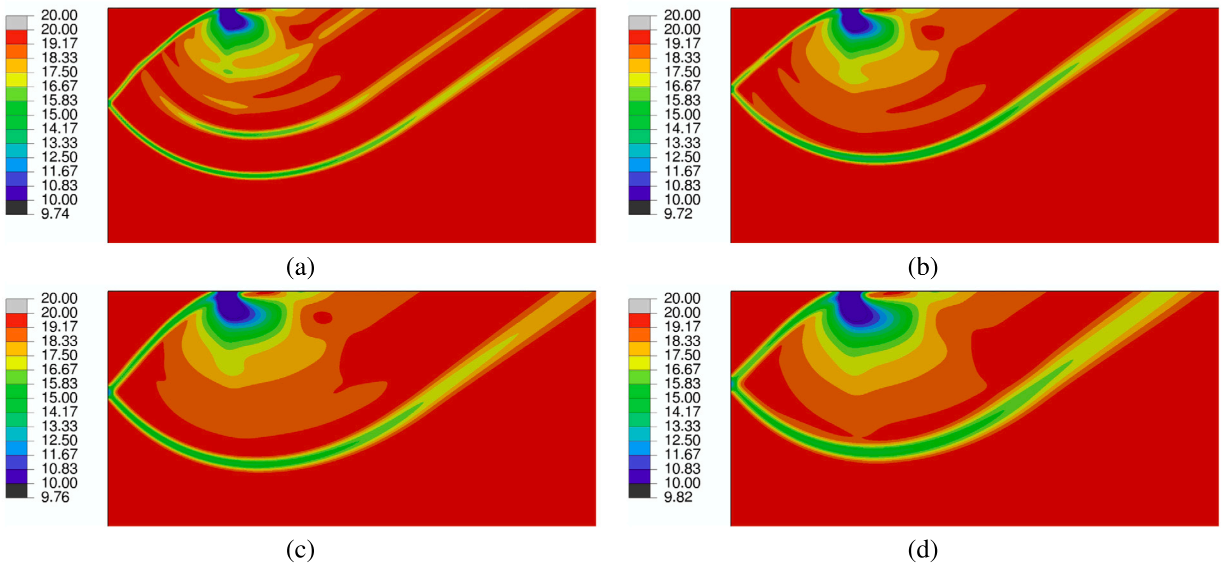

Fig. 19. Spatial distribution of the angle of shearing resistance ϕ (in degrees) for different values of $r = \ell/B$, at intermediate load (point A in Fig. 16, at $F_2/(Bh\kappa_0) \approx 18.75$) for Mesh 3. (a) $r = 4.5 \cdot 10^{-4}$, (b) $r = 6 \cdot 10^{-4}$, (c) $r = 8 \cdot 10^{-4}$, (d) $r = 10^{-3}$.

the classical limit analysis mechanism, with a relatively diffuse deformation field developing in the region between them. These results clearly indicate that the internal length does not merely affect the thickness of the shear bands, but fundamentally controls the selection of the deformation mechanisms. In particular, decreasing r promotes the activation of multiple competing localization modes, whereas larger values of r favor the emergence of simpler, more classical failure mechanisms.

The computational cost associated with different values of the internal length is reported in Table 5 for Mesh 3. In contrast to the previous table, which considered the effect of mesh refinement for a fixed value of r, the present data compare different values of $r = \ell/B$ on the same mesh. The results do not show a systematic increase of the computational cost as r decreases: the number of loading steps remains between 357 and 378, the total number of iterations remains between 795 and 850, and the total arc length varies only mildly. These results indicate that, despite the different localization patterns and the unstable post-peak behavior

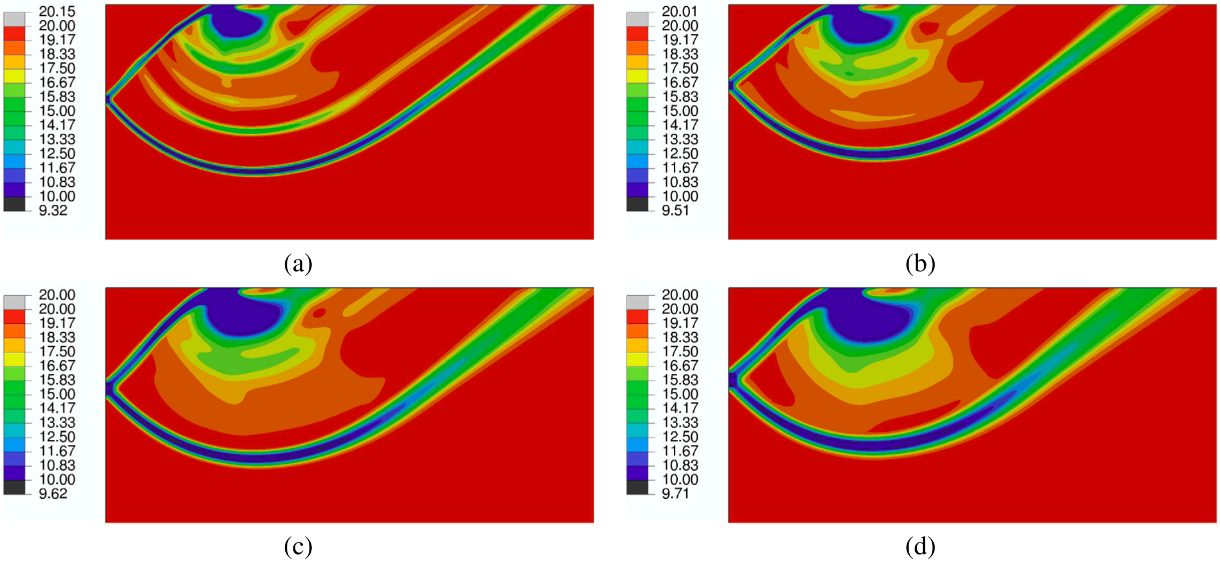

Fig. 20. Spatial distribution of the angle of shearing resistance ϕ (in degrees) for different values of $r = \ell/B$, at intermediate load (point C in Fig. 16, at $F_2/(Bh\kappa_0) \approx 14$), for Mesh 3. (a) $r = 4.5 \cdot 10^{-4}$, (b) $r = 6 \cdot 10^{-4}$, (c) $r = 8 \cdot 10^{-4}$, (d) $r = 10^{-3}$.

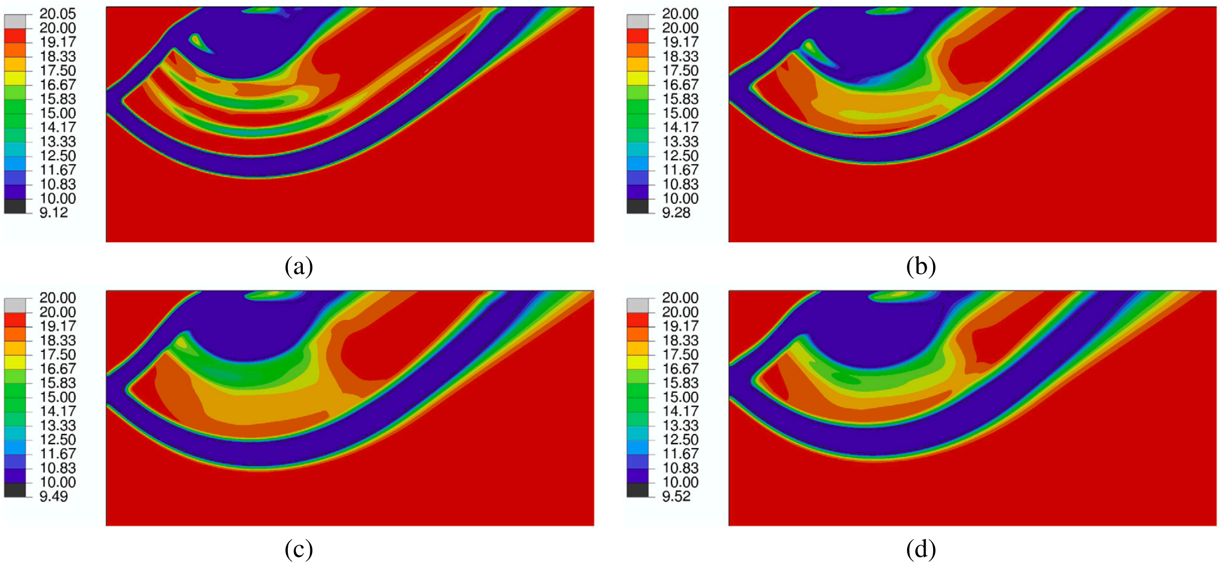

Fig. 21. Spatial distribution of the angle of shearing resistance ϕ (in degrees) for different values of $r = \ell/B$, at the last increment ($\bar{u}/B \approx 0.05$, point L in Fig. 16), for Mesh 3. (a) $r = 4.5 \cdot 10^{-4}$, (b) $r = 6 \cdot 10^{-4}$, (c) $r = 8 \cdot 10^{-4}$, (d) $r = 10^{-3}$.

observed in the Matsuoka–Nakai softening problem, the Riks procedure remains stable and computationally efficient for all internal lengths considered.

Overall, the results obtained for the Matsuoka–Nakai model with softening highlight the capability of the proposed formulation to robustly capture highly nonlinear responses, including pronounced softening and unstable behavior. The convergence of both global quantities and localization patterns confirms the mesh-objective nature of the approach, even in the presence of complex and evolving deformation mechanisms. At the same time, the analysis of different values of the internal length ℓ shows that the model does not merely regularize the solution, but actively governs the selection of the deformation modes. In particular, smaller values of ℓ promote the activation of multiple interacting shear bands and a strongly unstable response, whereas larger values lead to simpler mechanisms, closer to the classical limit analysis solution.

These findings demonstrate that, for the constitutive models here considered, the proposed framework provides a consistent and efficient tool for the analysis of strain localization in softening plasticity, combining robustness, mesh objectivity, and the ability to

Table 5
Computational cost for the Matsuoka–Nakai model with softening of the angle of shearing resistance, obtained using the Riks procedure for Mesh 3 and different values of $r = \ell/B$. The solution procedure remains stable and very efficient.

r	Loading steps	Total iterations	Total arc length
$4.5 \cdot 10^{-4}$	361	850	1.75
$6 \cdot 10^{-4}$	378	846	1.85
$8 \cdot 10^{-4}$	357	795	1.74
10^{-3}	369	817	1.80

reproduce a wide range of regularized deformation patterns controlled by the constitutive length scale without modifying standard constitutive models.

5. Discussion: How the model works

The mechanism by which the deformable Cosserat model influences localization can be understood by examining when the micro-continuum is activated and how it affects the response.

The additional (i.e., non-standard) micro-stress $\mathbf{T}_{\text{micro}}$ does not depend on macroscopic deformation alone, but on the *mismatch* between the directors $\mathbf{d}_i$ and the material line elements $\mathbf{a}_i$. This *mismatch* is described by the symmetric second-order tensor χ, which measures the corresponding relative strain between the macro and micro-continua. Thus, the deformable Cosserat model can be considered as the *dual* of the standard rigid Cosserat model, where the micro-stress depends only on the *relative rotation* between a *rigid* director triad (Panteghini & Lagioia, 2022b) and the macro-continuum.[7] A further analogy with the rigid Cosserat model concerns the higher-order kinematics. In the rigid setting, the curvature measure is defined by the gradient of the total director rotation. Similarly, in the present formulation, the curvature is determined by the gradient of the total director field $\boldsymbol{\eta}$. Thus, in both cases, the micro-stress is governed by a *relative* measure, whereas the micro-couples are determined by the gradients of the *total* micro-kinematic fields.

The rigid and deformable Cosserat models share the same director-based philosophy and, in this sense, both are axiomatic-deductive continuum models, just as is the classical Cauchy continuum. The essential difference lies in the constitutive choices made possible by the richer kinematics of the deformable model. In the present formulation, this richer kinematics makes it possible to adopt a purely energetic micro-continuum, while still obtaining a strong coupling through the balance of linear momentum and boundary conditions, and a robust regularization of localization. The additional degrees of freedom should therefore not be viewed as an unnecessary complication, but as the price paid for this stronger interaction between macro- and micro-response. This interpretation is also consistent with the numerical results: in the perfectly plastic benchmark problems, the introduction of the internal length does not dramatically alter either the main collapse mechanisms or the global load–displacement response relative to the classical Cauchy solution, while in the softening regimes investigated here it introduces a constitutive length scale that controls the regularized deformation field and predicts localization patterns whose evolution is mesh-independent for fixed values of the internal length.

If no explicit constitutive coupling is introduced, the interaction between the macro- and micro-continua is governed only by the balance of linear momentum and the corresponding boundary conditions. In both models, the balance of director momentum couples the micro-stress to the divergence of the micro-couples, whereas the balance of linear momentum involves the total stress. In the rigid Cosserat case, since the micro-stress is purely skew-symmetric, the coupling enters the balance of linear momentum only through the skew-symmetric part of the total stress. In the deformable Cosserat case, by contrast, the micro-stress is symmetric, which couples directly with the symmetric macro-stress to obtain the symmetric total stress. The resulting stronger coupling through the balance equations is sufficient, in the present model, to make it possible to retain a completely standard macro-elastoplastic description, in which dissipation depends only on the symmetric macro-stress and on the corresponding symmetric plastic deformation rates, while, in the numerical examples considered, still avoiding mesh-dependent localization.

In the rigid Cosserat case, the weaker coupling through the kinematics and the balance equations typically makes it necessary, in softening elastoplasticity, to formulate constitutive models in which the micro-stress, and especially the micro-couples, enter explicitly into the yield function and plastic potential (Mühlhaus & Vardoulakis, 1987; Panteghini & Lagioia, 2022b; Russo et al., 2020) in order to activate gradient effects (Russo et al., 2020) and mitigate mesh dependence when localization occurs. In contrast, the stronger coupling between macro- and micro-continua in the deformable Cosserat model can provide an effective regularizing mechanism without introducing plasticity in the micro-continuum, as shown by the benchmark problems considered in this work.

A further important feature of the deformable Cosserat model concerns the behavior of the micro-continuum under homogeneous deformation. In this case, the micro-continuum becomes inactive: the balance of director momentum (4) enforces $\mathbf{d}_i = \mathbf{a}_i$ and hence $\chi = \mathbf{0}$, while the balance of linear momentum involves only the macro-stress. The response, therefore, coincides with that of the standard macro-continuum.

[7] It should be noted, however, that the deformable Cosserat model adopted here does not include the rigid Cosserat model as a special case, although both reduce to the classical Cauchy continuum in the limit as the material length $\ell \to 0$ (Panteghini & Rubin, 2026).

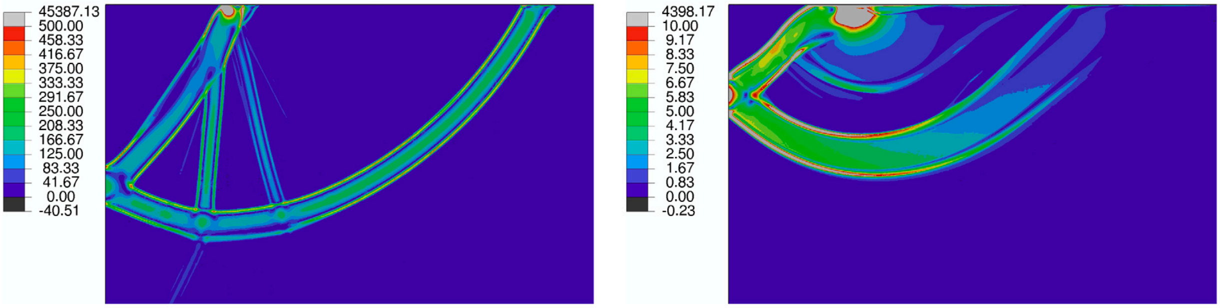

(a) (b)

Fig. 22. Spatial distribution of the modulus of the micro-stress $\sqrt{\mathbf{T}_{\text{micro}} : \mathbf{T}_{\text{micro}}}$ (in kPa) at the end of loading, for $r = 10^{-3}$. (a) Tresca soil with softening. (b) Matsuoka–Nakai soil with softening. In both cases, the micro-stress is negligible in the bulk of the domain and becomes significant only in narrow regions localized along the edges of the shear bands. Since $\mathbf{T}_{\text{micro}}$ is linearly related to the symmetric relative strain tensor $\boldsymbol{\chi} = \boldsymbol{\varepsilon} - \boldsymbol{\eta}$, the figure provides a direct indication of the regions where $\boldsymbol{\chi} \neq \mathbf{0}$, i.e., where the directors $\mathbf{d}_i$ differ from the material line elements $\mathbf{a}_i$.

This is exactly what is observed in Fig. 22: the micro-continuum becomes significant only in localized zones, where strong spatial variations of the strain field induce non-zero values of $\boldsymbol{\chi}$, i.e., a mismatch between the directors $\mathbf{d}_i$ and the material line elements $\mathbf{a}_i$. Accordingly, $\mathbf{T}_{\text{micro}}$ is negligible in the bulk and becomes significant only in narrow regions near the shear bands.

To better understand the role of the micro-stress in regularizing solutions, it is useful to relate the present reduced formulation to the Helmholtz-type micromorphic regularization mechanisms discussed by Forest (2016). Motivated by that work, it is convenient to separate the tensors $(\boldsymbol{\varepsilon}, \boldsymbol{\chi})$ into their spherical and deviatoric parts

$$
\begin{aligned}
\boldsymbol{\varepsilon} &= \frac{1}{3}\varepsilon_{\text{v}}\mathbf{I} + \boldsymbol{\varepsilon}' , \qquad \varepsilon_{\text{v}} = \boldsymbol{\varepsilon} : \mathbf{I} , \\
\boldsymbol{\chi} &= \frac{1}{3}\chi_{\text{v}}\mathbf{I} + \boldsymbol{\chi}' , \qquad \chi_{\text{v}} = \boldsymbol{\chi} : \mathbf{I} .
\end{aligned}
\tag{55}
$$

Then, with the help of (11), (12) and (17) and recalling that, in the reduced formulation, $\boldsymbol{\eta} = \boldsymbol{\varepsilon} - \boldsymbol{\chi}$, it can be shown that

$$
\operatorname{div} \mathbf{M}^i \otimes \mathbf{e}_i = \frac{4}{3} G \ell^2 \nabla^2 (\varepsilon_{\text{v}} - \chi_{\text{v}})\mathbf{I} + 4 G \ell^2 \nabla^2 (\boldsymbol{\varepsilon}' - \boldsymbol{\chi}') . \tag{56}
$$

and that the balance of director momentum (4) requires

$$
\nabla^2 \chi_{\text{v}} - \left(\frac{3k_1}{4\ell^2}\right)\chi_{\text{v}} = \nabla^2 \varepsilon_{\text{v}} , \qquad \nabla^2 \boldsymbol{\chi}' - \left(\frac{k_2}{4\ell^2}\right)\boldsymbol{\chi}' = \nabla^2 \boldsymbol{\varepsilon}' ,
$$

where $\nabla^2(\cdot) = (\cdot)_{,kk}$ is the Laplacian operator. These equations show that the spherical and deviatoric parts of the relative strain $\boldsymbol{\chi}$ are governed by Helmholtz-type relations driven by the Laplacian of the corresponding parts of the macro-strain. As discussed by Forest (2016), the positivity of (k_1, k_2, ℓ) is an essential property of the model for obtaining a regularizing Helmholtz-type response. Accordingly, under homogeneous deformation and in the absence of boundary-induced microstructural effects, $\boldsymbol{\chi} = \mathbf{0}$ and the micro-stress vanishes. During localization, instead, strong spatial variations of the strain field act as source terms in the above equations, activating $\boldsymbol{\chi}$ and hence the micro-stress $\mathbf{T}_{\text{micro}}$.

This provides a direct interpretation of the plots of $\mathbf{T}_{\text{micro}}$: the micro-continuum remains essentially inactive in regions where the variations in the strain field are small, whereas it becomes significant near localization zones, where strain gradients and director curvatures develop.

The preceding relations make the regularization mechanism explicit. In a standard softening continuum, no comparable energetic mechanism opposes the collapse of localization into an arbitrarily narrow zone, so that the computed band thickness is ultimately governed by the discretization. Here, by contrast, sharply localized kinematics require non-zero relative strain $\boldsymbol{\chi}$ and non-zero director curvatures, each of which carries an energetic cost. The collapse into a zero-width zone therefore becomes energetically unfavorable, and the localization pattern develops over a finite width controlled by the constitutive length-scale parameter ℓ rather than by the mesh.

It is emphasized that the present mechanism is fundamentally different from approaches in which an internal length is introduced at the constitutive level through a length-dependent effective measure governed by additional differential equations, such as phase field, gradient plasticity or other nonlocal models.

This also clarifies the role of the internal length ℓ. Rather than acting as a numerical regularization parameter, ℓ governs the characteristic width and spatial extent of the regions where these gradients are energetically penalized. For a fixed value of ℓ, the numerical results presented here show convergence towards well-defined localization patterns upon mesh refinement, while varying ℓ leads to qualitatively different responses in both the global behavior and the associated shear band structures. Thus, the role of ℓ is not merely to smooth the numerical solution, but to control a mechanically meaningful localization width and, consequently, a mesh-objective regularized response in the boundary-value problems considered. These observations support interpreting ℓ as a constitutive material length-scale parameter, to be identified from experimental measurements of shear-band thickness and spatial deformation patterns. Classical biaxial tests specifically designed to allow the spontaneous formation of shear bands in soils, such as those of Vardoulakis and Goldscheider (1981), provide a relevant experimental setting in which such information could be obtained. A direct calibration of ℓ against such experimental shear-band data is beyond the scope of the present numerical study and is left for future work. The extension of these conclusions to other softening laws, constitutive models, and boundary-value problems should be assessed on a case-by-case basis.

The stronger regularization capability of the deformable Cosserat model is not obtained for free. Compared to the rigid Cosserat model, the present formulation introduces additional degrees of freedom and requires constitutive choices for the micro-continuum, including the identification of the parameters (k_1, k_2, ℓ). Moreover, for small values of the internal length, converged localization patterns may require very fine spatial resolution. In this respect, adaptive meshing strategies guided by the magnitude of the micro-stress $\mathbf{T}_{\mathrm{micro}}$ appear to be a natural direction for future work. More generally, the present study has been carried out within the small-strain setting, and the numerical implementation of the corresponding finite-strain theory of Rubin and Panteghini (2026) remains an important open step for the analysis of fully developed localization.

The role of the internal length also deserves a precise interpretation. Different values of ℓ may affect the detailed structure of the localization pattern, in particular in terms of the number and richness of secondary shear bands. Specifically, once the value of ℓ is sufficiently small to predict the dominant shear bands, further reduction of ℓ leaves these dominant shear bands relatively unchanged, while exposing a finer structure of evolving patterns. In this sense, the internal length should not be viewed as introducing arbitrary mechanisms, but rather as controlling the scale at which the localization process is resolved.

Finally, the computational cost of the present approach should not be judged only in terms of the additional degrees of freedom. One of its main practical advantages is that the underlying macro-constitutive model can be used as a true black-box component, without modifying the stress update algorithm or the consistent tangent operator. In a computational environment involving many constitutive models, this may substantially reduce development, implementation, and debugging effort, even if the final boundary-value problem remains more expensive at the discrete level.

6. Conclusions

This paper has investigated strain localization in softening plasticity by means of the small-strain specialization of the deformable Cosserat model proposed by Rubin and Panteghini (2026), and has presented a finite element implementation of the resulting formulation.

The deformable Cosserat model consists of two interacting continua: a macro-continuum and a micro-continuum. Their constitutive responses are uncoupled, whereas their interaction is governed by the balances of linear and director momentum and by the associated boundary conditions. The macro-continuum governs the entire dissipative response and is described by a standard elastoplastic constitutive law. The micro-continuum is non-dissipative and contributes only through additional energetic terms associated with the mismatch between the directors and material line elements, as well as with the corresponding director curvatures. It therefore becomes relevant only when sufficiently strong spatial variations of the strain field develop, and governs the structure of the resulting localization patterns.

The main advantage of the proposed approach is that, because of this constitutive structure, standard elastoplastic constitutive laws developed for the classical Cauchy continuum can be employed for the macro-continuum without any modification of either the local stress-update algorithm or the local material consistent tangent operator.

A key aspect of the proposed formulation is that the stronger kinematic coupling provided by the deformable-director setting is sufficient to influence localization without introducing plasticity at the micro-level. This distinguishes the present approach both from the rigid Cosserat model, where the coupling is weaker and typically requires a more direct constitutive involvement of micro-stresses and micro-couples, and from gradient-enhanced or nonlocal formulations, in which the internal length is introduced directly through the constitutive description.

The resulting finite element implementation is particularly simple. The macro-response is obtained from a standard constitutive update driven by the symmetric part of the displacement gradient rate $\mathbf{D}$, exactly as in a standard Cauchy continuum. All the quantities associated with the micro-continuum, namely the symmetric relative strain tensor χ, the director curvatures, the micro-stresses, and the micro-couples, are then determined explicitly from the nodal values of $\mathbf{u}$ and the symmetric tensor $\boldsymbol{\eta}$ through the finite element operators and linear elastic relations. Hence, once the macro-stress and the corresponding local material consistent elastoplastic tangent have been obtained from a standard constitutive routine, the remaining part of the formulation reduces to the assembly of linear contributions. A general finite element algorithm has been presented, together with the corresponding FE operators for the plane strain case. This opens the possibility of extending the approach to a broad class of standard constitutive models without reformulating their constitutive integration algorithms.

The performance of the proposed approach has been assessed through a boundary value problem known to be particularly demanding, namely the shallow foundation problem under plane strain conditions. Tresca and Matsuoka–Nakai plasticity models have been considered, including both perfectly plastic and softening responses. In the softening regime, for the two constitutive models considered and for a fixed value of the constitutive material length-scale parameter ℓ, the proposed formulation yields mesh-independent solutions with localization patterns that converge upon mesh refinement. In particular, for the Matsuoka–Nakai model, convergence is also obtained in cases exhibiting unstable post-peak behavior. At the same time, varying ℓ leads to qualitatively different responses, both in terms of global behavior and of the associated shear-band profiles.

The present study has been carried out within the small-strain setting. This is sufficient for assessing in the considered setting, whether the proposed deformable Cosserat framework can regularize localization and produce converged mesh-independent patterns while preserving a standard macro-elastoplastic constitutive structure. However, once localization is fully developed, the deformation inside the narrow localized regions may become too large for the small-strain approximation to remain quantitatively accurate. In such cases, the appropriate framework is the nonlinear finite-strain theory developed in the companion paper (Rubin & Panteghini, 2026), whose numerical implementation is outside the scope of the present work.

The numerical results support the conclusion that the proposed model is a mechanically meaningful framework for the description of evolving strain localization patterns in softening plasticity, while preserving the practical simplicity of standard elastoplastic constitutive updates at the macro-continuum level.

CRediT authorship contribution statement

Andrea Panteghini: Writing – review & editing, Writing – original draft, Visualization, Validation, Software, Resources, Project administration, Methodology, Investigation, Formal analysis, Conceptualization. **M.B. Rubin:** Writing – review & editing, Writing – original draft, Visualization, Validation, Resources, Project administration, Methodology, Investigation, Funding acquisition, Conceptualization.

Declaration of competing interest

The authors declare that they have no known competing financial interests or personal relationships that could have appeared to influence the work reported in this paper.

Acknowledgments

The finite element code Simulia Abaqus has been run at the Department of Civil, Environmental, Architectural Engineering and Mathematics, University of Brescia, Italy, under an academic license

Appendix. Finite element operators for the plane strain formulation

The matrix $\mathbf{H}_r$ that contains the derivatives of the shape functions for displacements and geometry with respect to the intrinsic coordinate system $\boldsymbol{r}$, can be expressed as

$$\mathbf{H}_r = \begin{bmatrix} \frac{\partial N^{(1)}}{\partial r} & .. & \frac{\partial N^{(n)}}{\partial r} \\ \frac{\partial N^{(1)}}{\partial s} & .. & \frac{\partial N^{(n)}}{\partial s} \end{bmatrix}. \tag{A.1}$$

In the same way, the matrix $\mathbf{H}_{\eta r}$ that contains the derivatives of the shape functions for the tensor components η_{ij} with respect to the intrinsic coordinate system $\boldsymbol{r}$, can be expressed as

$$\mathbf{H}_{\eta r} = \begin{bmatrix} \frac{\partial N_\eta^{(1)}}{\partial r} & .. & \frac{\partial N_\eta^{(n_\eta)}}{\partial r} \\ \frac{\partial N_\eta^{(1)}}{\partial s} & .. & \frac{\partial N_\eta^{(n_\eta)}}{\partial s} \end{bmatrix}. \tag{A.2}$$

The Jacobian can be computed as

$$\boldsymbol{J} = \mathbf{H}_r \hat{\mathbf{X}}, \tag{A.3}$$

where

$$\hat{\mathbf{X}} = \begin{bmatrix} \hat{x}_1^{(1)} & \hat{x}_2^{(1)} \\ .. & .. \\ \hat{x}_1^{(n)} & \hat{x}_2^{(n)} \end{bmatrix}. \tag{A.4}$$

The nodal displacements are ordered in the vector $\hat{\mathbf{u}}$ of $2n$ components

$$\hat{\mathbf{u}} = \begin{bmatrix} \hat{u}_1^{(1)} & \hat{u}_2^{(1)} & .. & \hat{u}_1^{(n)} & \hat{u}_2^{(n)} \end{bmatrix}^T.$$

Since the micro-distortion tensor $\boldsymbol{\eta}$ is symmetric, only its symmetric components are retained as independent primary variables. In the plane strain formulation the Voigt-type array has been employed:

$$\hat{\boldsymbol{\eta}} = \begin{bmatrix} \hat{\eta}_{11}^{(1)} & \hat{\eta}_{22}^{(1)} & 2\hat{\eta}_{12}^{(1)} & .. & \hat{\eta}_{11}^{(n_\eta)} & \hat{\eta}_{22}^{(n_\eta)} & 2\hat{\eta}_{12}^{(n_\eta)} \end{bmatrix}^T. \tag{A.5}$$

The second-order identity tensor, in array notation, has the form

$$\mathbf{I} = \begin{bmatrix} 1 & 1 & 1 & 0 \end{bmatrix}^T, \tag{A.6}$$

while the operator $\mathcal{I}^{v}_{\text{dev}}$ denotes the deviatoric projection written in the Voigt notation adopted for strain-like arrays:

$$\mathcal{I}^{v}_{\text{dev}} = \begin{bmatrix} \frac{2}{3} & -\frac{1}{3} & -\frac{1}{3} & 0 \\ -\frac{1}{3} & \frac{2}{3} & -\frac{1}{3} & 0 \\ -\frac{1}{3} & -\frac{1}{3} & \frac{2}{3} & 0 \\ 0 & 0 & 0 & \frac{1}{2} \end{bmatrix}. \tag{A.7}$$

The standard strain–displacement operator $\mathcal{B}$ is obtained from the derivatives of the shape functions with respect to the physical coordinates. It maps the nodal displacement vector into the engineering strain array

$$\boldsymbol{\varepsilon} = \begin{bmatrix} \varepsilon_{11} \\ \varepsilon_{22} \\ \varepsilon_{33} \\ 2\varepsilon_{12} \end{bmatrix} = \mathcal{B}\hat{\mathbf{u}}, \tag{A.8}$$

where

$$\mathcal{B} = \begin{bmatrix} (\mathbf{H})_{11} & 0 & \cdots & (\mathbf{H})_{1n} & 0 \\ 0 & (\mathbf{H})_{21} & \cdots & 0 & (\mathbf{H})_{2n} \\ 0 & 0 & \cdots & 0 & 0 \\ (\mathbf{H})_{21} & (\mathbf{H})_{11} & \cdots & (\mathbf{H})_{2n} & (\mathbf{H})_{1n} \end{bmatrix}. \tag{A.9}$$

The operator $\mathcal{N}_\eta$ maps the shape functions $\mathbf{N}_\eta$ into a $4 \times 3n_\eta$ matrix, which is defined by

$$\mathcal{N}_\eta = \begin{bmatrix} N_\eta^{(1)} & 0 & 0 & .. & N_\eta^{(n_\eta)} & 0 & 0 \\ 0 & N_\eta^{(1)} & 0 & .. & 0 & N_\eta^{(n_\eta)} & 0 \\ 0 & 0 & 0 & .. & 0 & 0 & 0 \\ 0 & 0 & N_\eta^{(1)} & .. & 0 & 0 & N_\eta^{(n_\eta)} \end{bmatrix}. \tag{A.10}$$

The operator $\mathcal{G}_\eta$ maps the components of $\mathbf{H}_\eta$ into a $8 \times 3n_\eta$ matrix, which is defined by:

$$\mathcal{G}_\eta = \begin{bmatrix} (\mathbf{H}_\eta)_{11} & 0 & 0 & \cdots & (\mathbf{H}_\eta)_{1n_\eta} & 0 & 0 \\ 0 & (\mathbf{H}_\eta)_{11} & 0 & \cdots & 0 & (\mathbf{H}_\eta)_{1n_\eta} & 0 \\ 0 & 0 & \frac{1}{2}(\mathbf{H}_\eta)_{11} & \cdots & 0 & 0 & \frac{1}{2}(\mathbf{H}_\eta)_{1n_\eta} \\ 0 & 0 & \frac{1}{2}(\mathbf{H}_\eta)_{11} & \cdots & 0 & 0 & \frac{1}{2}(\mathbf{H}_\eta)_{1n_\eta} \\ (\mathbf{H}_\eta)_{21} & 0 & 0 & \cdots & (\mathbf{H}_\eta)_{2n_\eta} & 0 & 0 \\ 0 & (\mathbf{H}_\eta)_{21} & 0 & \cdots & 0 & (\mathbf{H}_\eta)_{2n_\eta} & 0 \\ 0 & 0 & \frac{1}{2}(\mathbf{H}_\eta)_{21} & \cdots & 0 & 0 & \frac{1}{2}(\mathbf{H}_\eta)_{2n_\eta} \\ 0 & 0 & \frac{1}{2}(\mathbf{H}_\eta)_{21} & \cdots & 0 & 0 & \frac{1}{2}(\mathbf{H}_\eta)_{2n_\eta} \end{bmatrix}. \tag{A.11}$$

Thus,

$$\mathcal{G}_\eta \hat{\boldsymbol{\eta}} = \begin{bmatrix} \eta_{11,1} \\ \eta_{22,1} \\ \eta_{12,1} \\ \eta_{21,1} \\ \eta_{11,2} \\ \eta_{22,2} \\ \eta_{12,2} \\ \eta_{21,2} \end{bmatrix}, \qquad \eta_{12,k} = \eta_{21,k}. \tag{A.12}$$

Data availability

Data will be made available on request.

References

Anand, L. (2026). Fracture of rock-like materials: A gradient-damage theory. *International Journal of Solids and Structures*, *325*, Article 113739. http://dx.doi.org/10.1016/j.ijsolstr.2025.113739.

Bažant, Z. P., & Jirásek, M. (2002). Nonlocal integral formulations of plasticity and damage: Survey of progress. *Journal of Engineering Mechanics*, *128*(11), 1119–1149. http://dx.doi.org/10.1061/(ASCE)0733-9399(2002)128:11(1119).

Bažant, Z. P., & Pijaudier-Cabot, G. (1988). Nonlocal continuum damage, localization instability and convergence. *Journal of Applied Mechanics*, *55*(2), 287–293. http://dx.doi.org/10.1115/1.3173674.

Chambon, R., Caillerie, D., & Matsuchima, T. (2001). Plastic continuum with microstructure, local second gradient theories for geomaterials: Localization studies. *International Journal of Solids and Structures*, *38*(46), 8503–8527. http://dx.doi.org/10.1016/S0020-7683(01)00057-9.

Cosserat, E. M. P., & Cosserat, F. (1909). *Théorie des corps déformables*. A. Hermann et fils.

Dassault Systèmes (2024). *ABAQUS user's & theory manuals — Release 6.24*. Providence, RI, USA.

de Borst, R. (1991). Simulation of strain localization: A reappraisal of the Cosserat continuum. *Engineering Computations*, *8*(4), 317–332. http://dx.doi.org/10.1108/eb023842.

de Borst, R., & Sluys, L. (1991). Localisation in a Cosserat continuum under static and dynamic loading conditions. *Computer Methods in Applied Mechanics and Engineering*, *90*(1), 805–827. http://dx.doi.org/10.1016/0045-7825(91)90185-9.

de Borst, R., & Vermeer, P. A. (1984). Possibilities and limitations of finite elements for limit analysis. *Géotechnique*, *34*(2), 199–210. http://dx.doi.org/10.1680/geot.1984.34.2.199.

de Souza Neto, E. A., Peric, D., & Owen, D. R. J. (2008). *Computational methods for plasticity*. Chichester, UK: John Wiley & Sons, Ltd.

Dillard, T., Forest, S., & Ienny, P. (2006). Micromorphic continuum modelling of the deformation and fracture behaviour of nickel foams. *European Journal of Mechanics. A. Solids*, *25*(3), 526–549. http://dx.doi.org/10.1016/j.euromechsol.2005.11.006.

Duda, F. P., Ciarbonetti, A., Sánchez, P. J., & Huespe, A. E. (2015). A phase-field/gradient damage model for brittle fracture in elastic–plastic solids. *International Journal of Plasticity*, *65*, 269–296. http://dx.doi.org/10.1016/j.ijplas.2014.09.005.

Duretz, T., Räss, L., de Borst, R., & Hageman, T. (2023). A comparison of plasticity regularization approaches for geodynamic modeling. *Geochemistry, Geophysics, Geosystems*, *24*(7), http://dx.doi.org/10.1029/2022GC010675.

Ebrahimian, H., Pietruszczak, S., & Vardoulakis, I. (2012). Modeling shear localization along granular soil-structure interfaces using elasto-plastic Cosserat continuum. *International Journal of Solids and Structures*, *49*(19–20), 2797–2809. http://dx.doi.org/10.1016/j.ijsolstr.2011.09.005.

Eckart, C. (1948). The thermodynamics of irreversible processes. IV. The theory of elasticity and anelasticity. *Physical Review*, *73*, 373–382. http://dx.doi.org/10.1103/PhysRev.73.373.

Eringen, A. C., & Suhubi, E. S. (1964). Nonlinear theory of simple micro-elastic solids–I. *International Journal of Engineering Science*, *2*(2), 189–203. http://dx.doi.org/10.1016/0020-7225(64)90004-7.

Forest, S. (2009). Micromorphic approach for gradient elasticity, viscoplasticity, and damage. *Journal of Engineering Mechanics*, *135*(3), 117–131. http://dx.doi.org/10.1061/(ASCE)0733-9399(2009)135:3(117).

Forest, S. (2016). Nonlinear regularization operators as derived from the micromorphic approach to gradient elasticity, viscoplasticity and damage. *Proceedings of the Royal Society of London, Series A*, *472*(2188), Article 20150755. http://dx.doi.org/10.1098/rspa.2015.0755.

Forest, S. (2020a). Continuum thermomechanics of nonlinear micromorphic, strain and stress gradient media. *Proceedings of the Royal Society of London, Series A*, *378*(2170), Article 20190169. http://dx.doi.org/10.1098/rsta.2019.0169.

Forest, S. (2020b). Micromorphic approach to materials with internal length. In H. Altenbach, & A. Öchsner (Eds.), *Encyclopedia of continuum mechanics* (pp. 1643–1652). Berlin, Heidelberg: Springer Berlin Heidelberg, http://dx.doi.org/10.1007/978-3-662-55771-6_150.

Forest, S., & Sievert, R. (2006). Nonlinear microstrain theories. *International Journal of Solids and Structures*, *43*(24), 7224–7245. http://dx.doi.org/10.1016/j.ijsolstr.2006.05.012.

Jirásek, M. (2003). Comparison of integral-type nonlocal plasticity models for strain-softening materials. *International Journal of Engineering Science*, *41*(13–14), 1553–1602. http://dx.doi.org/10.1016/S0020-7225(03)00027-2.

Khoei, A., & Karimi, K. (2008). An enriched-FEM model for simulation of localization phenomenon in Cosserat continuum theory. *Computational Materials Science*, *44*(2), 733–749. http://dx.doi.org/10.1016/j.commatsci.2008.05.019.

Khoei, A., Yadegari, S., & Biabanaki, S. (2010). 3D finite element modeling of shear band localization via the micro-polar Cosserat continuum theory. *Computational Materials Science*, *49*(4), 720–733. http://dx.doi.org/10.1016/j.commatsci.2010.06.015.

Lade, P. V., & Duncan, J. M. (1974). Elasto Plastic stress–strain theory for cohesionless soil. *Journal of the Geotechnical Engineering Division, American Society of Civil Engineers*, *101*(GT10), 1037–1053. http://dx.doi.org/10.1061/AJGEB6.0000204.

Lagioia, R., & Panteghini, A. (2016). On the existence of a unique class of yield and failure criteria comprising Tresca, von Mises, Drucker–Prager, Mohr–Coulomb, Galileo–Rankine, Matsuoka–Nakai and Lade-Duncan. *Proceedings of the Royal Society of London, Series A*, *472*(2185), Article 20150713. http://dx.doi.org/10.1098/rspa.2015.0713.

Lagioia, R., & Panteghini, A. (2017). Accounting for specific failure criteria in the slip-line method for plane strain problems. *Géotechnique Letters*, *7*(2), 184–189. http://dx.doi.org/10.1680/jgele.17.00014.

Leonov, A. I. (1976). Nonequilibrium thermodynamics and rheology of viscoelastic polymer media. *Rheologica Acta*, *15*, 85–98. http://dx.doi.org/10.1007/BF01517499.

Lorentz, E. (2011). Gradient damage models: Toward full-scale computations. *Computer Methods in Applied Mechanics and Engineering*, *200*(1–4), 90–109. http://dx.doi.org/10.1016/j.cma.2010.07.015.

Martin, C. M. (2003). New software for rigorous bearing capacity calculations. In *Proc. international conference on foundations* (pp. 581–592).

Martin, C. M. (2004). *User guide for ABC-analysis of bearing capacity version 1.0 department of engineering science university of Oxford*, (no. 2261).

Matsuoka, H., & Nakai, T. (1974). Stress-deformation and strength characteristics of soil under three different principal stresses. *Proceedings of the Japan Society of Civil Engineers*, *1974*(232), 59–70.

Miehe, C., Aldakheel, F., & Teichtmeister, S. (2017). Phase-field modeling of ductile fracture at finite strains: A robust variational-based numerical implementation of a gradient-extended theory by micromorphic regularization. *International Journal for Numerical Methods in Engineering*, *111*(9), 816–863. http://dx.doi.org/10.1002/nme.5484.

Miehe, C., Hofacker, M., & Welschinger, F. (2010). A phase field model for rate-independent crack propagation: Robust algorithmic implementation based on operator splits. *Computer Methods in Applied Mechanics and Engineering*, *199*(45–48), 2765–2778. http://dx.doi.org/10.1016/j.cma.2010.01.008.

Miehe, C., Welschinger, F., & Hofacker, M. (2010). Thermodynamically consistent phase-field models of fracture in elastic solids. *International Journal for Numerical Methods in Engineering*, *83*(10), 1273–1311. http://dx.doi.org/10.1002/nme.2861.

Mindlin, R. D. (1964). Microstructure in linear elasticity. *Archive of Rational Mechanics*, *16*, 51–78. http://dx.doi.org/10.1007/BF00248490.

Mühlhaus, H.-B., & Vardoulakis, I. (1987). The thickness of shear bands in granular materials. *Géotechnique*, *37*(3), 271–283. http://dx.doi.org/10.1680/geot.1987.37.3.271.

Needleman, A., & Tvergaard, V. (1992). Analyses of plastic flow localization in metals. *Applied Mechanics Reviews*, *45*(3S), S3–S18. http://dx.doi.org/10.1115/1.3121390.

Panteghini, A., & Lagioia, R. (2014). A fully convex reformulation of the original Matsuoka–Nakai failure criterion and its implicit numerically efficient integration algorithm. *International Journal for Numerical and Analytical Methods in Geomechanics*, *38*(6), 593–614. http://dx.doi.org/10.1002/nag.2228.

Panteghini, A., & Lagioia, R. (2018). An approach for providing quasi-convexity to yield functions and a generalized implicit integration scheme for isotropic constitutive models based on 2 unknowns. *International Journal for Numerical and Analytical Methods in Geomechanics*, *42*(6), 829–855. http://dx.doi.org/10.1002/nag.2767.

Panteghini, A., & Lagioia, R. (2022a). An implicit integration algorithm based on invariants for isotropic elasto-plastic models of the Cosserat continuum. *International Journal for Numerical and Analytical Methods in Geomechanics*, *46*(12), 2233–2267. http://dx.doi.org/10.1002/nag.3386.

Panteghini, A., & Lagioia, R. (2022b). A micropolar isotropic plasticity formulation for non-associated flow rule and softening featuring multiple classical yield criteria. *International Journal for Numerical and Analytical Methods in Geomechanics*, *46*(4), 674–696. http://dx.doi.org/10.1002/nag.3316.

Panteghini, A., & Rubin, M. B. (2026). On the evolution of damage-induced localization in a deformable-director Cosserat continuum. *Computer Methods in Applied Mechanics and Engineering*, *453*, Article 118797. http://dx.doi.org/10.1016/j.cma.2026.118797.

Peerlings, R. H. J., de Borst, R., Brekelmans, W. A. M., & de Vree, J. H. P. (1996). Gradient enhanced damage for quasi-brittle materials. *International Journal for Numerical Methods in Engineering*, *39*(19), 3391–3403. http://dx.doi.org/10.1002/(SICI)1097-0207(19961015)39:19<3391::AID-NME7>3.0.CO;2-D.

Peerlings, R. H. J., de Borst, R., Brekelmans, W. A. M., & de Vree, J. H. P. (1998). Gradient-enhanced damage modelling of concrete fracture. *Engineering Fracture Mechanics*, *60*(1), 1–12. http://dx.doi.org/10.1016/S0013-7944(97)00117-9.

Perić, D., Yu, J., & Owen, D. (1994). On error estimates and adaptivity in elastoplastic solids: Applications to the numerical simulation of strain localization in classical and Cosserat continua. *International Journal for Numerical Methods in Engineering*, *37*(8), 1351–1379. http://dx.doi.org/10.1002/nme.1620370806.

Prandtl, L. (1920). Uber die Harte Plastischer Korper. *Nachrichten Von der Koeniglichen Gesellschaft der Wissenschaften Zu Goettingen, Mathematisch-Physikalische Klasse*, 74–85.

Rubin, M. B. (2025a). Correction to: A thermomechanical Eulerian formulation of a size-dependent elastic-inelastic Cosserat continuum. *Journal of Elasticity*, *157*(77), http://dx.doi.org/10.1007/s10659-025-10173-1.

Rubin, M. B. (2025b). A thermomechanical Eulerian formulation of a size-dependent elastic-inelastic Cosserat continuum. *Journal of Elasticity*, *157*(12), http://dx.doi.org/10.1007/s10659-024-10105-5.

Rubin, M. B. (2026). On the balance of angular momentum and the balances of director momentum in a deformable Cosserat continuum. *Journal of Elasticity*, *158*, http://dx.doi.org/10.1007/s10659-026-10213-4.

Rubin, M. B., & Panteghini, A. (2026). An Eulerian deformable Cosserat model for large deformations of porous geomaterials. *Journal of Elasticity* (submitted for publication).

Russo, G., Forest, S., & Girot-Mata, C. (2020). Thermomechanics of Cosserat media: Modeling adiabatic shear bands in metals. *Continuum Mechanics and Thermodynamics*, *32*, 1051–1076. http://dx.doi.org/10.1007/s00161-020-00930-z.

Sabet, S. A., & de Borst, R. (2019a). Mesh bias and shear band inclination in standard and non-standard continua. *Archive of Applied Mechanics*, *89*(12), 2577–2590. http://dx.doi.org/10.1007/s00419-019-01593-2.

Sabet, S. A., & de Borst, R. (2019b). Structural softening, mesh dependence, and regularisation in non-associated plastic flow. *International Journal for Numerical and Analytical Methods in Geomechanics*, *43*(13), 2170–2183. http://dx.doi.org/10.1002/nag.2973.

Sharbati, E., & Naghdabadi, R. (2006). Computational aspects of the Cosserat finite element analysis of localization phenomena. *Computational Materials Science*, *38*(2), 303–315. http://dx.doi.org/10.1016/j.commatsci.2006.03.003.

Suhubi, E. S., & Eringen, A. C. (1964). Nonlinear theory of micro-elastic solids–II. *International Journal of Engineering Science*, *2*(4), 389–404. http://dx.doi.org/10.1016/0020-7225(64)90017-5.

Vardoulakis, I., & Goldscheider, M. (1981). Biaxial apparatus for testing shear bands in soils. In *Proceedings, 10th ICSMFE*: *vol. 4/61*, (pp. 819–824).